Dynamics of Earth's Hadley Circulation

Thesis by

Xavier J. Levine

In Partial Fulfillment of the Requirements

for the Degree of

Doctor of Philosophy

California Institute of Technology

Pasadena, California

2013

(Defended November 15th, 2012)

Hâtez-vous lentement; et, sans perdre courage,

Vingt fois sur le métier remettez votre ouvrage.

L'Art Poétique (1674), Canto I,

Nicolas Boileau-Despréaux

Acknowledgements

This work would not have been possible without the help and support of my family, my group members, my advisor, and many more people from the Caltech community.

First, I would like to thank my parents, Pierre and Sophie, for their constant support throughout these years. I am very grateful to have had such open-minded parents, who have always been supportive of my academic endeavors. I also would like to thank my brother Philippe for having been a steady companion during these years, in better and worst times, including during my first few years in California. I am also indebted to Odilie Boegner, for being such an affectionate grand-mother and being such a kind host for my many stays in Chamonix. At last, but certainly not least, I have been extremely lucky to have known my other grandparents, Jean-Marc Boegner, Anne-Marie Levine, and Simon Levine, who sadly are not here today but have exemplified moral integrity and kindness in my regards. I also have a special thought for Muscade for being such a good-hearted companion during my stay in France for so many years.

The Caltech community has been an amazing place to learn; there, I had the privilege of meeting many gifted friends. I would like to particularly thank Tim Merlis and Tobias Bischoff for providing me with many great discussions, which contributed significantly to shaping me as a better scientist. I also would like to acknowledge other friends, in

particular postdocs: first, Paul O'Gorman for being such a great support in my early phase in grad school. Yohai Kaspi, who has helped me through the highs and lows of grad-school with his (scientific) advise and his humor. Ian Eisenman, for providing very insightful comments on my articles and proposals, and for being Skipper's owner! I would like to acknowledge other group members, in particular Junjun Liu, Cheikh Mbengue, Alejandro Soto and Zhihong Tan. Caltech would not be such a special place without the exceptional administrative support I enjoyed during my time, and most particularly by Nora Oshima, Liz Muira Boyd, and Dian Buchness. At least, but certainly not the least, I have a special recognition for the french mafia at Caltech: first, Fabien Paulot, with whom I have shared so many good times and was a tremendous support during my first 5 years; Farid Ait-Chalal, who provided very insightful advise on my research and has helped me keeping sane despite the heavy workload; Remi Lam, who shared his knowledge on clouds and many fun times with me.

I am very grateful to Tapio Schneider for greatly improving the quality of my work, and for being always very supportive of my work. Many other people have contributed to my academic experience at Caltech; I would like to mention in particular Simona Bordoni for her very insightful advice on research and non-research topics, as well as her constant support. Finally, but not the least, I would like to thank every member of my thesis committee [Tapio Schneider (Advisor), Simona Bordoni (Chair), Andy Ingersoll and Paul Wennberg] for their time and effort in improving the research presented in this thesis.

Abstract

This thesis advances our understanding of the mechanisms controlling the Hadley circulation, and its interaction with eddies on planetary scales in particular. On Earth, and more generally in a rapidly rotating and differentially heated planet, large-scale eddies in the extratropics interact with the mean flow in the tropics, contributing to the driving of the Hadley circulation. A hierarchy of numerical models is used to simulate and understand the relative importance of the eddies in the driving of the Hadley circulation. In a global warming experiment, the Hadley circulation is found to strengthen in colder climates and weaken in warmer climates, with a maximum strength in a climate close to present-day Earth's. This nonmonotonicity is shown to be consistent with variations in the eddy activity in the midlatitudes. The cells are also found to widen over the entire range of this climate change. A criterion quantifying the importance of baroclinic waves in setting the depth of the troposphere, which is modified to account for the effect of convective adjustment on planetary Rossby waves activity, is used to explain the shifts in the terminus of the Hadley circulation for a wide range of climate scenarios. Additionally, by comparing simulations with and without ocean heat transport, it is shown that accounting for low-latitude ocean heat transport and its coupling to wind stress is essential to obtain Hadley circulations in a dynamical regime resembling Earth's. These changes in the strength and extent are found to be captured in a simple one-dimensional model that relies on standard assumptions about the thermodynamic properties of the atmosphere in the low-latitude regions and with a simple representation of eddy fluxes. Further work with this model, which may be amenable to analytical progress, could provide a quantitative understanding for the sensitivity of the Hadley circulation in comprehensive GCM simulations of 21st century global warming scenarios.

Contents

List of Figures

List of Tables

Chapter 1

Introduction

1.1 Overview of the Hadley circulation

Earth's low-latitude climate is shaped by the Hadley circulation, an overturning circulation that dominates the poleward transport of heat, momentum, and moisture in the tropics. This circulation extends to about 30° latitude in both hemispheres and occupies the entire troposphere, i.e., the lowest 80% of the atmosphere in mass. Averaged over a year, it is organized into two cells that advect air masses poleward in the upper troposphere and equatorward near the surface in a nearly symmetric pattern about the equator.

Predicting how this circulation may respond to an increase in greenhouse gas concentrations is required for assessing the impact of global warming on human societies and ecosystems in the low latitudes. Indeed, the strength of the mass transport and the poleward extent of the Hadley circulation control many aspects of the surface climate, e.g., the extent of the trade winds and the location and extent of the arid zones in the subtropics. Any change in the width or strength of the Hadley circulation has important implications, for example, for the atmospheric hydrologic cycle by inducing poleward shifts of the subtropical arid zones as the climate warms (Seager et al., 2007). Yet it is not understood how the Hadley circulation responds to climate changes, and models and observations do not agree on the magnitude of the response.

A Hadley circulation also exists on other planetary bodies, when covered by an atmosphere. In some cases, this circulation has shaped prominent land features: on Titan, for instance, lake networks in the polar regions (Stofan et al., 2007) were found to be consistent with the existence of a cross-hemispheric Hadley circulation that reverses seasonally (Mitchell et al., 2006; Schneider et al., 2012) .

Observations on Earth show a widening and a strengthening of the Hadley circulation, especially since the 1970s. Mass flux estimates from reanalysis datasets suggest that the Hadley circulation has widened by about 1.1° per decade between 1979 and 2005 (Hu and Fu, 2007). The Hadley circulation may also have strengthened over the past 30 years, as suggested by changes in outgoing longwave radiation (OLR) measured from the Earth Radiation Budget Experiment (ERBE) (Chen et al., 2002). Reanalysis data likewise indicate a strengthening by more than 15% over the same period (Mitas and Clement, 2005). Evidence suggests that changes in the dynamics of the Hadley circulation is linked to drastic changes in the surface climate in the past: for instance, the subtropical regions of North Africa have experienced large hydrologic swings since the Last Glacial Maximum (Gasse and Roberts, 2004).

Observational trends over the past 30 years are inconsistent with either GCM hindcasts or forecasts. In global warming scenarios for the 21st century, comprehensive GCM simulations predict a widening of about 0.5° and a weakening of about 1.2% per 1 K global-mean surface temperature increase (Lu et al., 2007). But the climate sensitivity inferred from reanalysis and OLR datasets is much higher for the past 30 years, with a widening of more than 6.0° and a strengthening of more than 40% per 1 K global mean surface temperature increase. This glaring discrepancy cannot be explained by any of the known anomalous forcings that occurred in the last decades of the 20th century (Johanson and Fu, 2009), but it seems to result from systematic biases in either (or both) reanalysis datasets or GCM simulations. This is corroborated by the fact that the widening of the Hadley circulation is an order of magnitude smaller in GCM hindcasts with prescribed sea surface temperature than in reanalysis datasets (Johanson and Fu, 2009; Mitas and Clement, 2005). It is unclear why the trends in the GCM simulations and reanalysis datasets differ so dramatically. On one hand, systematic errors in retrieving tropospheric temperature from radiosondes (Santer et al., 2005; Sherwood, 2007) may have strongly biased the strengthening and widening trends in reanalysis data. On the other hand, reanalysis and OLR datasets, which have been obtained independently, show a comparable widening (Hu and Fu, 2007; Johanson and Fu, 2009). Hence, it is not clear that instrumental artifacts are responsible for the large trends in observational datasets.

1.2 Theoretical approaches

The trends neither in the strength nor in the width are currently understood. Indeed, the complex driving mechanism of the Hadley circulation has challenged our ability to build a comprehensive theory. In the simplest theory (e.g., Held and Hou, 1980), the Hadley circulation is depicted as a set of thermally driven and laminar cells, which responds directly to changes the thermal drivings. This, however, is a poor model even for the tropics, where eddies play a major role in the driving of the Hadley circulation (Walker and Schneider, 2006).

A laminar axisymmetric circulation cannot exist in a real (three-dimensional) atmosphere, as the large zonal wind vertical shear predicted in this regime would be unstable to linear baroclinic instability (e.g., Held, 2000). On Earth, the spatial structure and lifecycle of this instability not only provide a fair description of the weather systems that develop in the storm track regions, but baroclinic waves are actually found to control the static stability in these stormy regions (e.g., Schneider, 2006). The effects of these waves on the dynamics is not confined, however, to the storm track regions: they have a major influence on the tropical atmosphere as well, by exerting a stress on the zonal flow (Becker and Schmitz, 2001; Kim and Lee, 2001; Walker and Schneider, 2006) and inducing a poleward transport of heat and moisture in the low-latitude regions (e.g., Trenberth and Caron, 2001).

The relative importance of thermal drivings compared to the eddy stresses defines the flow regime of the Hadley circulation, which is bounded by two ideal limits. The first limit corresponds to a thermally driven and eddy-free Hadley circulation (e.g., Held and Hou, 1980). The other limit corresponds to an eddy-driven circulation, in which the strength responds directly to changes in eddy stresses (e.g., Dickinson, 1971). In the eddy-driven limit, the Hadley circulation is slaved to storminess in the midlatitudes, as extratropical weather systems largely control the eddy stress in the tropics. In the present climate, the flow regime in low latitudes varies between the eddy-free or eddy-driven regime (Walker and Schneider, 2005; Schneider and Bordoni, 2008).

The terminus of the Hadley circulation is a boundary between regions where the depth of the troposphere is set by baroclinic waves in the storm tracks regions, and regions where the depth of the troposphere is set by convection in the deep tropics; defining this transition is an important step toward understanding what controls the location of the Hadley circulation terminus in the present climate, and what drives its poleward shift in global warming scenarios. A criterion was found to characterize successfully this transition in dry atmospheres (Schneider and Walker, 2006). But its applicability to moist atmospheres is unclear (Schneider and O'Gorman, 2008), and inconsistencies remain even when it is modified to account for the effect of latent heat release in cyclonic updrafts (O'Gorman, 2010).

In addition, existing theories do not account for the low-latitude ocean heat transport, although its effect on the Hadley circulation is critical (Herweijer et al., 2005; Lee et al., 2008; Schneider et al., 2010). The zonal surface wind stress within the Hadley circulation induces an ocean circulation with upwelling in the deep tropics, poleward flow near the surface, downwelling in the subtropics, and an equatorward return flow in the thermocline (Lu et al., 1998; McCreary Jr. and Lu, 1994). This meridional overturning cell dominates the low-latitude ocean heat transport (Held, 2001; Klinger and Marotzke, 2000), which in turn dominates the meridional energy transport in the ocean–atmosphere system in the tropics (Trenberth and Caron, 2001). By reducing the surface temperature gradient there, the ocean heat transport directly impacts the strength and extent of the Hadley circulation and their trends as the climate changes. In the present climate, the importance of ocean heat transport in the tropics implies that it must be accounted for in any model seeking to describe Earth's circulation and its variations with climate changes.

1.3 Models

The climate range covered by comprehensive GCM simulations, such as those used for climate prediction in the IPCC reports, remains limited. Comprehensive GCMs are seldom used for simulating climate changes of large amplitude. Indeed, their complex representation of unresolved processes is partially empirical (for instance, their cloud scheme) and tuned to provide a best fit with our present climate. But there is generally little confidence in their behavior in a very different climate. In addition, they increase the computational cost of a GCM, which severely limits the number of simulations that can be conducted. Both the narrow climate range and the small number of simulations are impairing our ability to test theories of the Hadley circulation.

1.3.1 General circulation model (GCM)

To address this issue, we use an idealized GCM, i.e., a GCM with the simplest possible representation of unresolved processes and the smallest number of free parameters. Processes that are poorly understood (for instance, cloud effects) are ignored in the idealized GCM. This class of models is less successful at reproducing the present-day climate than are comprehensive GCMs, but the fewer degrees of freedom make them more reliable for simulating large-scale features of extreme climates while improving computing performance. The aim of an idealized GCM is not to attempt a precise prediction of climate changes on Earth, but to inform us about the component of climate changes most directly controlled by large-scale dynamics. Understanding climate change in this idealized atmosphere is a first step before adding clouds and other complex physics. Here we have used a moist idealized atmosphere GCM, described in O'Gorman and Schneider (2008b), and a dry idealized atmosphere GCM, described in Walker and Schneider (2006). These models already resolve eddy stresses, in addition to an idealized representation of heat sources in the atmosphere. We also add in the moist GCM a representation of ocean heat transport in low latitudes derived by Klinger and Marotzke (2000), which describes the ocean heat transport by the wind-driven meridional overturning circulation.

1.3.2 Single-layer model (SLM)

The driving of the Hadley circulation is complex as it is strongly influenced by both thermal drivings and eddy stresses. To make progress toward a theory for the strength and extent of the Hadley circulation, we drastically simplify the dynamics of the atmosphere, in a manner consistent with well-known properties of low-latitude regions. For instance, we assume that the tropopause height and the lapse rate are constant in latitude, which is consistent with the weak temperature gradient approximation (Sobel et al., 2001) and the lapse rate being set by moist convection (e.g., Arakawa and Schubert, 1974). In addition, both the thermal drivings and the eddy stresses are given a simple representation, which varies with climate and will be derived from the GCM simulations, similar to the study by Sobel and Schneider (2009) (see also Xian and Miller, 2008). This single-layer model has four principal external parameters: (i) tropopause height, (ii) moisture content, (iii) thermal gradient established by insolation, and (iv) a parameter measuring extratropical storminess. These external parameters are varied to change the climate in the single-layer model, with the ultimate goal of deriving analytical scaling laws for the Hadley circulation. This model allows for an idealized representation of ocean heat transport, which shall be added latter.

1.4 Thesis outline

To build a theory for the sensitivity of the Hadley circulation to climate changes, we propose a three-stage approach using both the idealized GCMs and a single-layer model. In the first chapter, we address how the Hadley circulation and its coupled ocean heat transport respond to climate changes. In the second chapter, we modify a criterion comparing the depth of baroclinic waves and that of the troposphere to diagnose the terminus of the Hadley circulation in dry and moist atmospheres alike. In the third chapter, we build a simple conceptual model that is designed to capture the essential physics of low-latitude climate changes; preliminary results from this model shows it can capture climate changes as observed in the GCM simulations. It also sheds light on the primary sensitivity of the Hadley circulation, in particular what controls changes in its strength and width. We hope that further work based on these results will help build a theory adapted to Earth's dynamics based on a mechanistic understanding of the Hadley circulation, which in turn can be used to investigate the discrepancy between GCM simulations and observational datasets.

Chapter 2

Response of the Hadley Circulation to Climate Change in an Aquaplanet GCM Coupled to a Simple Representation of Ocean Heat Transport

2.1 Introduction

The Hadley circulation appears to have widened in the past decades (Hu and Fu, 2007; Seidel and Randel, 2007; Seidel et al., 2008), and it also widens in many global-warming simulations (Lu et al., 2007; Seager et al., 2007). It may also have strengthened, though the evidence for a significant strengthening is ambiguous (Quan et al., 2004; Chen et al., 2002; Mitas and Clement, 2005). In global-warming simulations, the Hadley circulation weakens slightly in many models, but this is not consistent among all models (Tanaka et al., 2005). Trends in the Hadley circulation inferred from observational data are considerably larger than those obtained in comprehensive general circulation model (GCM) simulations (Mitas and Clement, 2005; Johanson and Fu, 2009). Depending on how it is measured, the widening appears to be nearly an order of magnitude larger in observations than in GCM simulations (Seidel et al., 2008). Yet it is unclear what instrumental or modeling artifact causes such large discrepancies in the response of the Hadley circulation to climate change; radiosonde data and their use in reanalysis models may be part of the problem (see, e.g., Santer et al., 2005; Sherwood, 2007).

Despite a large body of observations and numerous studies with GCMs, it remains unclear how the width and strength of the Hadley circulation are controlled (Schneider, 2006). Here we study how the width and strength of the Hadley circulation change over a wide range of climates simulated with an idealized GCM. This allows us to place possible changes in the Hadley circulation in a larger context and to determine whether, for example, the Hadley circulation generally widens as the climate warms, even in climates very different from the present. Our intention with these simulations is to provide a detailed target for the development of a Hadley circulation theory, but such a theory itself is beyond the scope of this chapter.

It is often assumed that the Hadley circulation responds directly to changes in thermal driving, in the sense that its changes are controlled by thermodynamic balances. For that to be the case, the balance of angular momentum about Earth's spin axis, or the balance of zonal momentum, would have to be degenerate in the upper troposphere, so that eddy momentum fluxes do not influence the Hadley circulation. In the upper troposphere, above the center of the Hadley cells where vertical momentum advection by the mean meridional circulation can be neglected, the mean zonal momentum balance may be used to quantify how strongly eddy momentum fluxes influence the mean meridional flow:

$$f(1 - \mathrm{Ro})\bar{v} \approx S_e. \tag{2.1}$$

Here, S_e is the eddy momentum flux divergence, f the planetary vorticity (Coriolis parameter), and v the meridional velocity; overbars indicate a temporal and zonal mean. The local Rossby number $\mathrm{Ro} = -\bar{\zeta}/f$, with relative vorticity ζ, is a nondimensional measure of the importance of nonlinear angular momentum advection by the mean meridional circulation (Walker and Schneider, 2006; Schneider, 2006). In the limit $\mathrm{Ro} \to 1$, the upper branch of the Hadley circulation conserves angular momentum and is unaffected by eddy momentum fluxes; its strength responds directly to changes in thermal driving. This is the limit considered in classical theories for the Hadley circulation, which provide expressions for its width and strength as a function of thermal and other parameters (Schneider, 1977; Held and Hou, 1980; Lindzen and Hou, 1988). In the limit $\mathrm{Ro} \to 0$, the strength of the Hadley circulation is controlled by eddy momentum fluxes; its strength responds to changes in thermal driving only insofar as they affect the eddy momentum fluxes (e.g., Dickinson, 1971). In between these limiting cases lie Hadley circulations with $0 < \mathrm{Ro} < 1$ in their upper branches, which respond to changes in thermal driving through changes in thermodynamic balances, in eddy momentum fluxes, and possibly in Rossby numbers. There is no theory that captures how the Hadley circulation responds to climate changes in this intermediate range of Rossby numbers.

Figure 2.1 shows the meridional mass flux streamfunction, the eddy momentum flux divergence, and the local Rossby number for Earth's atmosphere during equinox and in the annual mean. The quantities are similar during equinox and in the annual mean, suggesting that the annual mean is not dominated by an average of solstitial circulations (cf. Lindzen and Hou 1988; see also Dima and Wallace 2003; Walker and Schneider 2005). The eddy

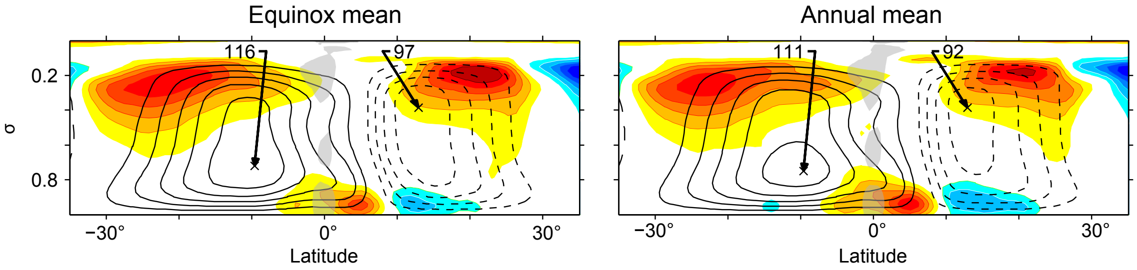

Figure 2.1: Earth's Hadley circulation (a) averaged over equinox seasons (MAM and SON) and (b) averaged annually. Black contours show the mass flux streamfunction, with dashed (negative) contours indicating clockwise motion and solid (positive) contours indicating counterclockwise motion (contour interval $25\,\mathrm{Sv} = 25 \times 10^9\,\mathrm{kg\,s^{-1}}$). Arrows indicate the streamfunction extremum in each hemisphere, with the magnitude given in $10^9\,\mathrm{kg\,s^{-1}}$. Colors indicate horizontal eddy momentum flux divergence $\mathrm{div}(\overline{u'v'}\cos\phi)$, with the overbar denoting a temporal and zonal mean and primes denoting deviations therefrom (that is, eddy fields include stationary and transient eddies). The contour interval for the eddy momentum flux divergence is $4 \times 10^{-6}\,\mathrm{m\,s^{-2}}$, with red tones for positive and blue tones for negative values; the darkest red tone corresponds to values greater than $2.4 \times 10^{-5}\,\mathrm{m\,s^{-2}}$. Gray shading indicates regions where $|\mathrm{Ro}| > 0.5$. Flow statistics are computed from reanalysis data for the years 1980–2001 provided by the European Centre for Medium-Range Weather Forecasts (Kallberg et al., 2004; Uppala et al., 2005).

momentum flux divergence has a broad maximum in the upper troposphere centered near 21° latitude, extending deep into the Hadley cells (color contours in Fig. 2.1). The Rossby number Ro in the upper troposphere gradually decreases from close to 1 at the equator to close to 0 in the subtropics, with values greater than 0.5 confined to a narrow band within $\sim 4^\circ$ latitude of the equator (gray shading in Fig. 2.1). Near the center of the Hadley cells (near 10° latitude), the Rossby number is between 0.35 and 0.45 during equinox and in the annual mean. This indicates that angular momentum–conserving theories are inadequate for describing Hadley cell dynamics, at least poleward of about 10° latitude during equinox and in the annual mean. Understanding how eddy momentum fluxes change with climate therefore is integral to understanding how the Hadley circulation responds to climate changes. This is borne out in observational data and models, which show that interannual variations in the strength of Hadley cells and differences in their strength among climate models are correlated with the eddy momentum flux divergence in low latitudes (Caballero, 2007, 2008).

In addition to eddy momentum fluxes, the Hadley circulation is intimately linked to ocean heat transport, which dominates the total meridional energy transport in the ocean–atmosphere system at low latitudes (Trenberth and Caron, 2001). The ocean heat transport is coupled to the strength of the Hadley circulation: The Coriolis force on the meridional near-surface mass flux in the Hadley cells approximately balances the zonal surface wind stress (Ekman balance in the atmosphere). In turn, the zonal surface wind stress, by Ekman balance in the ocean, induces an ocean circulation with upwelling in the deep tropics, poleward flow near the surface, downwelling in the subtropics, and an equatorward return flow in the thermocline (McCreary Jr. and Lu, 1994; Lu et al., 1998). This meridional overturning cell dominates the low-latitude ocean heat transport and helps control the surface temperature near the equator (Klinger and Marotzke, 2000; Held, 2001) and the meridional surface temperature gradients (Trenberth and Solomon, 1994). It also dominates the total heat transport in the deep tropics because the Hadley circulation there is inefficient at transporting energy (e.g., Peixoto and Oort, 1992, chapter 13). Taking this heat transport into account is essential for obtaining Hadley circulations resembling Earth's. If it is neglected in simulations, meridional surface temperature gradients near the equator are generally too large, resulting in Hadley circulations that are too strong and often are closer to the angular momentum–conserving limit $\mathrm{Ro} \to 1$ than is Earth's Hadley circulation. This occurs, e.g., in the simulations in Herweijer et al. (2005) and Lee et al. (2008), potentially implying different responses to climate changes depending on whether ocean heat transport is taken into account or not.

We investigate how the Hadley circulation responds to climate changes with an idealized GCM coupled to a simple representation of ocean heat transport by a wind-driven low-latitude overturning circulation. We consider the case of insolation with no diurnal or seasonal cycle—the natural starting point for studies of the Hadley circulation, before considering the additional complexities of the seasonal cycle (e.g., Lindzen and Hou, 1988; Walker and Schneider, 2005; Schneider and Bordoni, 2008; Bordoni and Schneider, 2008). Inclusion of ocean heat transport allows us to obtain Hadley circulations with strengths, Rossby numbers, and widths resembling those of Earth, and coupling it to the surface wind stress and thus to the strength of the Hadley circulation allows us to take into account feedbacks between the atmosphere and low-latitude oceans. Using this GCM, we simulate a wide range of climates by varying the longwave optical thickness of the atmosphere. We compare these simulations with simulations performed by O'Gorman and Schneider (2008b) that are otherwise identical but do not include ocean heat transport. We show that the Hadley circulation generally widens as the climate warms but that it does not necessarily weaken, both in the simulations with ocean transport and in those of O'Gorman and Schneider without ocean heat transport. We analyze the dynamics involved in the changes in some detail, to provide a target for the development of theories to account for them. (O'Gorman and Schneider focused on the hydrologic cycle and did not analyze Hadley circulation dynamics in detail. Here we analyze their simulations along with the ones without ocean heat transport.)

2.2 Idealized GCM

2.2.1 Atmosphere

The atmospheric GCM is a primitive-equation model with idealized representations of radiative transfer (a gray radiation scheme) and moist thermodynamics (only the vapor-liquid phase transition of water is taken into account). It is based on the Flexible Modeling System (FMS) developed at the Geophysical Fluid Dynamics Laboratory (GFDL). The model is described in detail in O'Gorman and Schneider (2008b); it is similar to the model described in Frierson et al. (2006) and Frierson (2007). Here we only give a brief overview.

The GCM solves the primitive equations in vorticity-divergence form, using the spectral-transform method in the horizontal (Bourke, 1974) and finite differences in the vertical (Simmons and Burridge, 1981). We use a horizontal resolution of T42 and 30 vertical sigma levels, unevenly spaced to better resolve dynamics in the uppermost and lowermost part of the troposphere. To damp small scales, scale-selective ∇^8 hyperdiffusion is included in the vorticity, divergence, and temperature equations, with a hyperdiffusion coefficient chosen such that the damping timescale for the smallest resolved scale is 12 h.

The lower boundary of the GCM is uniform and water covered, with an albedo of 0.38. A planetary boundary layer scheme with Monin-Obhukov surface fluxes, which depend on the stability of the boundary layer, links atmospheric dynamics to surface fluxes of momentum, latent heat, and sensible heat. The roughness length for momentum fluxes is 5×10^{-3} m but that for latent and sensible heat fluxes is reduced to 10^{-5} m, to obtain energy fluxes and a climate similar to Earth's in the aquaplanet setting of our simulations.

Radiative transfer is represented by a two-stream gray radiation scheme with longwave and shortwave optical depths that only depend on latitude and pressure. The longwave absorption in this scheme can be thought of as an idealized representation of the longwave absorption by water vapor and well-mixed greenhouse gases. However, the longwave optical thickness of the atmosphere is a fixed function of latitude, which we rescale to change the simulated climate, but which does not depend, for example, on the atmospheric concentration of water vapor in the model. Thus, we do not take water vapor feedback explicitly into account, but its effect can be viewed as included in the prescribed longwave optical thickness for a given climate. Moist convection is represented by a slightly modified version of the quasi-equilibrium convection scheme of Frierson (2007). It relaxes, with a timescale of 2 h, grid-scale temperature profiles toward a moist-adiabatic profile and water vapor profiles toward a profile with fixed relative humidity (70%), whenever a parcel lifted from the lowest model level is convectively unstable. Large-scale condensation removes water vapor from the atmosphere when the specific humidity on the grid scale exceeds the saturation specific humidity.

In addition to neglecting surface inhomogeneities such as land-ocean contrasts and topography, the GCM is idealized in that it neglects explicit representations of features such as sea ice, aerosols, and clouds (except insofar as their global-mean effect on Earth's albedo is implicitly taken into account in our choice of surface albedo).

2.2.2 Ocean

The surface wind stress from the atmosphere model drives a simple model of ocean heat transport in low latitudes. The ocean heat transport in the equatorial latitude band with surface easterlies is assumed to be accomplished by a wind-driven meridional overturning circulation, with poleward flow near the surface and an equatorward return flow in the thermocline. The Coriolis force on the poleward surface flow is in balance with the zonal surface wind stress (Ekman balance). The return flow is assumed to be adiabatic, so that water parcels conserve their temperature (neglecting salinity and compressibility effects) after subduction in the subtropics, until they upwell into the surface mixed layer in the deep tropics. Klinger and Marotzke (2000) showed that under these conditions, the meridional heat flux associated with the wind-driven ocean circulation can be expressed in terms of surface quantities (subscript s) as

$$\begin{aligned} F(\varphi) &= 2\pi a c_o \cos\varphi \int_{-H}^{0} \rho_o \bar{v}\,\bar{T}\,dz && (2.2) \\ &= 2\pi a c_o \cos\varphi \int_{\bar{T}_s(\varphi_h)}^{\bar{T}_s(\varphi)} \frac{\tau(\bar{T}_s)}{f}\,d\bar{T}_s. && (2.3) \end{aligned}$$

Here, $F(\varphi)$ is the meridional heat flux through a latitude (φ) circle, integrated from the surface to the ocean depth H, v is the meridional wind, T is the temperature, c_o is the specific heat, ρ_o is the density of the ocean, τ is the zonal surface wind stress, φ_h is the closest latitude to the equator at which zonal surface winds change sign (from easterlies to westerlies), and a is Earth's radius. Implicit in this formula is that the mean temperature of the subsurface return flow at latitude φ is expressed as the average surface temperature poleward of φ, with the average weighted by the strength of the downwelling Ekman mass flux at the poleward latitudes (Klinger and Marotzke, 2000; Held, 2001). This simple model of low-latitude ocean heat transport assumes laminar flow (no eddy mixing), with Ekman upwelling confined to the equator.

If this heat flux is coupled directly to the atmospheric GCM through the surface temperature and wind stress, it results in a local surface temperature minimum at the equator and a displacement of the ascending branches of the Hadley circulation a few degrees off the equator. Double ITCZs occur in coupled ocean-atmosphere GCMs and might be a natural state for an atmosphere-ocean system in perpetual equinox or in the annual mean. In our model, however, this ocean heat transport would imply excessive cooling at the equator, in part caused by assuming Ekman balance at the equator although the Coriolis parameter vanishes there. As a remedy, we apply a Gaussian smoothing filter to obtain the smoothed divergence of the meridional ocean heat transport,

$$\widetilde{\nabla \cdot F} = \int_{-\pi/2}^{\pi/2} \frac{1}{a \cos\varphi'} \partial_\varphi \left[F(\varphi') \cos\varphi' \right] P(\varphi, \varphi') \, d\varphi'. \tag{2.4}$$

Here,

$$P(\varphi, \varphi') = \frac{1}{Z} \exp\left[\frac{-(\varphi' - \varphi)^2}{2s^2} \right] \tag{2.5}$$

is a Gaussian smoothing function, with normalization factor Z chosen such that

$$\int_{-\pi/2}^{\pi/2} P(\varphi', \varphi) \, d\varphi' = 1. \tag{2.6}$$

We chose the standard deviation $s = 7^\circ$ for the smoothing filter.

The ocean heat transport in this representation is confined to the equatorial latitude band with surface easterlies (essentially the region of the Hadley circulation), which in the GCM is determined at every time step before the heat transport is calculated. In higher latitudes, the ocean heat transport vanishes, and the ocean is treated as a static thermal slab. The thermal inertia of the ocean is that of a water slab 0.5 m deep.

In a real ocean without lateral boundaries, to conserve momentum, a stress of equal magnitude but opposite sign as the surface stress would be required at the bottom of the ocean; this would generally mean that the meridional overturning circulation would have to close in a frictional bottom boundary layer, rather than in the thermocline (Haynes et al., 1991; O'Gorman and Schneider, 2008c). We will ignore this complication here and assume we can close the circulation within the thermocline with adiabatic flow.

2.2.3 Simulations

The GCM is forced by a quadratic representation of Earth's annual-mean insolation at the top of the atmosphere.This insolation is steady, i.e., there is no diurnal or seasonal cycle. Each simulation is run for more than 1000 days. Circulation statistics are averages of fields over the last 300 days, sampled 4 times daily, after a statistically steady state has been reached. Because the Northern and Southern Hemispheres in the simulations are statistically identical, hemispheric differences in the zonal- and time-mean fields shown in some of the figures are indicative of low-frequency sampling variability.

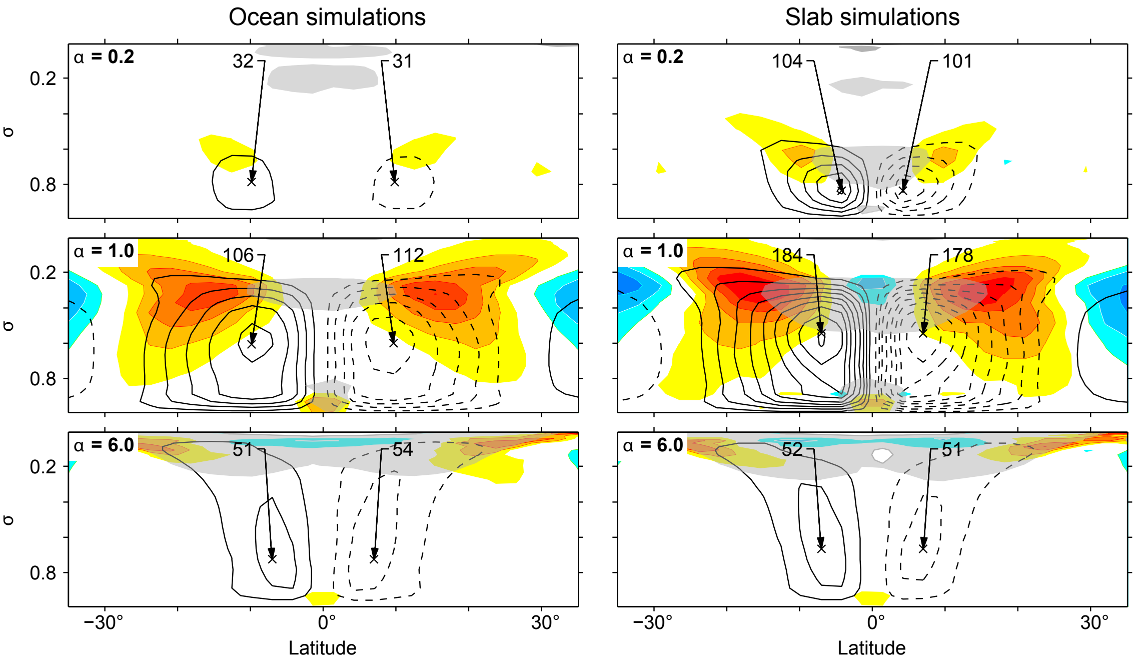

Figure 2.2: Mass flux streamfunction (black contours) and horizontal eddy momentum flux divergence $\mathrm{div}(\overline{u'v'}\cos\phi)$ (color contours). Plotting conventions and contour intervals as in Fig. 2.1. Rows show (top) the coldest ($\alpha = 0.2$), (middle) the reference ($\alpha = 1.0$), and (bottom) the warmest ($\alpha = 6.0$) simulation with ocean heat transport (left column) and without it (right column). Differences between the Northern and Southern Hemisphere are indicative of sampling variability.

2.3 Reference climate

To illustrate the impact of ocean heat transport on the low-latitude climate, we compare the climatology of the tropical atmosphere in reference simulations with the simple wind-coupled oceanic heat flux (“ocean simulation”) and without any ocean heat transport (“slab simulation”). Figure 2.2 (center row) show the mass flux streamfunction, eddy momentum flux divergence, and the Rossby number in the two reference simulations. The Hadley circulation mass flux in the ocean simulation is $109\,\mathrm{Sv}$, which compares very well with that of Earth in the annual mean ($102\,\mathrm{Sv}$), shown on Fig. 2.1. The mass flux is 66% stronger in the slab simulation than in the ocean simulation.

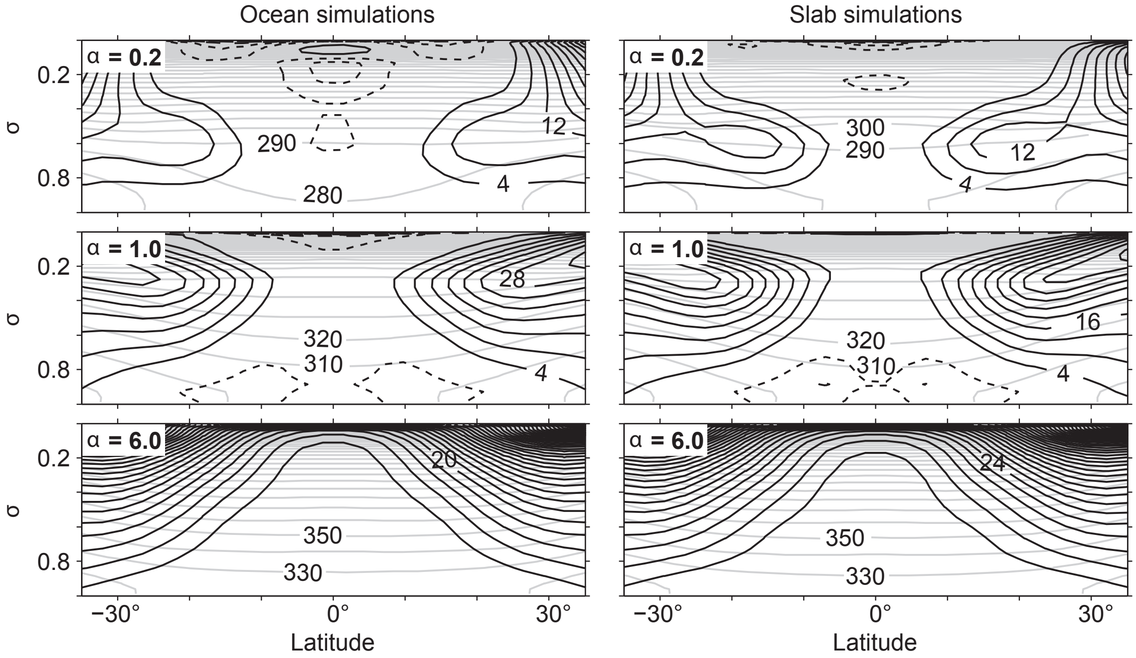

Figure 2.3: Mean zonal wind (black contours) and potential temperature (gray contours). Dashed black contours indicates easterlies and solid black contours indicates westerlies. Contour intervals are $4\,\mathrm{m\,s^{-1}}$ for zonal wind and $10\,\mathrm{K}$ for potential temperature. Rows show (top) the coldest ($\alpha = 0.2$), (middle) the reference ($\alpha = 1.0$), and (bottom) the warmest ($\alpha = 6.0$) simulation with ocean heat transport (left column) and without it (right column).

Ocean heat transport also decreases the Rossby number in the upper branch of the Hadley circulation, especially in the deep tropics. Figure 2.2 shows that the region of large Rossby number is smaller in the ocean simulation than in the slab simulation. The Rossby number in the deep tropics is also smaller in the ocean simulation. At the center of the Hadley circulation, the Rossby number in the ocean simulation (~ 0.4) is closer to Earth's in the annual mean (~ 0.3) than it is in the slab simulation (~ 0.6). This reduction in Rossby number implies changes in the mean zonal wind in the upper troposphere: Figure 2.3 (center row) shows a decrease in the strength of the subtropical jet, from $36\,\mathrm{m\,s^{-1}}$ in the slab simulation to $29\,\mathrm{m\,s^{-1}}$ in the ocean simulation. The eddy momentum flux divergence is also influenced by ocean heat transport, but to a lesser extent than the maximum mass flux streamfunction or the Rossby number. Figure 2.2 (center row) shows that, in the subtropics (poleward of 15° latitude), the mean poleward mass flux and the eddy momentum flux divergence, which are linearly related since Ro is small, differ by less than 25% between the two reference simulations. This demonstrates that the influence of ocean heat transport on the atmosphere is stronger in the deep tropics than in the subtropics, as expected given that the ocean heat flux is weak in the subtropics.

Ocean heat transport is the only process that we found is able to produce Hadley circulations with a strength and in a dynamical regime similar to Earth's. Otherwise, for instance, the radiative transfer formulation would have to be made unphysical (e.g., longwave optical thickness increasing away from the equator) to reduce the strength of the Hadley circulation to Earth-like values while leaving the eddy momentum flux divergence nearly unchanged. The necessity of including a representation of ocean heat transport is also seen in more comprehensive climate simulations, which otherwise produce unrealistically strong Hadley circulations (e.g., Herweijer et al., 2005).

2.4 Variations of climate

To investigate how the Hadley circulation responds to climate changes, we conducted series of simulations with and without ocean heat transport in which we varied the prescribed longwave optical thickness. Insolation at the top of the atmosphere and absorption of solar radiation within the atmosphere are kept fixed, so that the only changes in the energy budget come from changes in the longwave radiation (i.e., we do not take into account factors such as changes in the shortwave absorption owing to changes in the atmospheric concentration of water vapor). The longwave optical thickness is varied by rescaling the optical thickness in the reference simulation—a function of latitude and pressure—by a constant factor α as in O'Gorman and Schneider (2008b). Reducing the optical thickness ($\alpha < 1$) produces climates colder than the reference climate; increasing it ($\alpha > 1$) produces warmer climates. The rescaling factor α is set to 18 different values[1] ranging from 0.2 to 6.0. Each simulation is run for 1000 days. The simulated climates that result from these variations have global-mean surface temperatures between 260 and 315 K. The pole-to-equator surface temperature contrast decreases monotonically as the climate warms, in both the slab and ocean simulations, from $\sim$75 K in the coldest simulation to $\sim$23 K in the warmest simulation. The surface temperature contrast decreases largely because the poleward latent heat transport by eddies increases (O'Gorman and Schneider, 2008b).

2.4.1 Hadley circulation mass flux

2.4.1.1 Strength

In the simulations with ocean heat transport, the latitude φ_c of peak poleward mass flux in the upper branch of the Hadley circulation, or the extremum of the mass flux streamfunction, shifts equatorward as the climate warms, from 11.0° in the coldest simulation, 8.9° in the reference simulation, to 6.6° in the warmest simulation (Fig. 2.2, left column). In the simulations without ocean heat transport, it is closer to the equator and hardly changes as the climate warms, varying from 5.8° in the coldest simulation, 6.7° in the reference

---

[1] The values for α are 0.2, 0.3, 0.4, 0.5, 0.6, 0.7, 0.8, 0.9, 1.0, 1.2, 1.4, 1.6, 1.8, 2.0, 2.5, 3.0, 4.0, and 6.0.

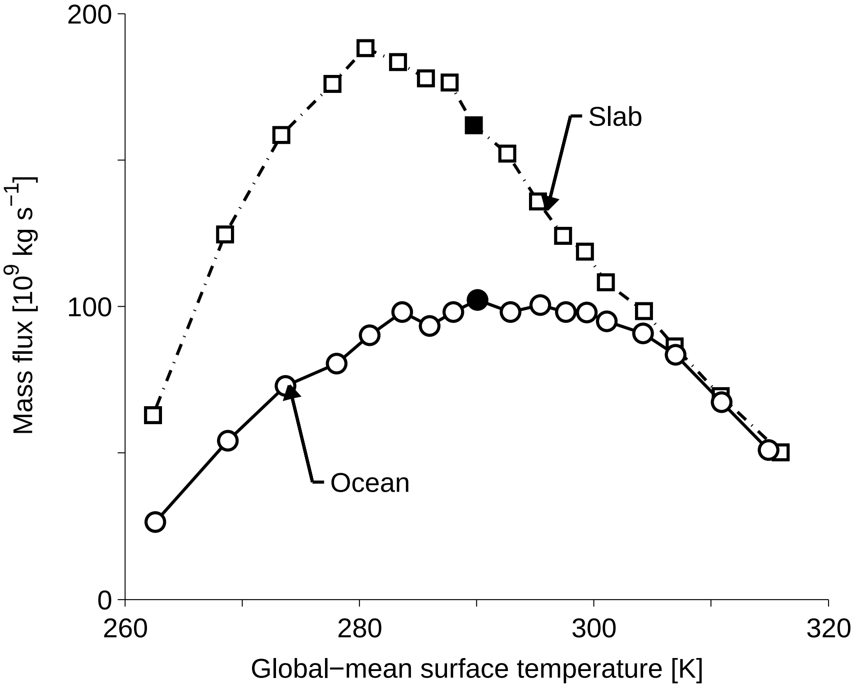

Figure 2.4: Strength of the Hadley circulation in simulations with (solid with circles) and without (dashed-dotted with squares) ocean heat transport. Shown is the absolute value of the mass flux streamfunction at the latitude of its extremum and at the level $\sigma_c = 0.7$, averaged over both hemispheres. Filled symbols identify the reference simulations in this and subsequent figures.

simulation, to $6.6°$ in the warmest simulation (Fig. 2.2, right column). On the other hand, it varies little in height, being confined between $\sim$500 and $\sim$700 hPa over the wide range of climates we simulated.

To compare the strength of the Hadley circulation over the entire range of climates we simulated, we compare the absolute values of the mass flux streamfunction evaluated at the (varying) latitude of the streamfunction extremum but at the (fixed) level $\sigma_c = 0.7$ (σ_c is the pressure at p_c normalized by its local value at the surface). Choosing the lowest level of the extremum of the mass flux streamfunction in the simulations for evaluation of the streamfunction reduces noise that would otherwise arise because of the vertical displacement of the center of the Hadley circulation. Figure 2.4 shows the results. As is already evident in Fig. 2.2, the Hadley circulation strength changes nonmonotonically with climate in both the ocean and slab simulations. In the ocean simulations, it is largest ($102\,\mathrm{Sv}$) in the reference climate ($\alpha = 1.0$, global-mean surface temperature 290 K) and is considerably lower in much colder and in much warmer climates. The behavior in the slab simulations is similar, although the maximum ($188\,\mathrm{Sv}$) occurs in a colder climate ($\alpha = 0.6$, global-mean surface temperature 281 K). The maximum is broader in the ocean simulations than in the slab simulations. For instance, the strength of the Hadley circulation varies by less than 15% of its maximum value for ocean simulations with global-mean surface temperatures between 281 and 304 K. This range of weak Hadley circulation sensitivity is narrower in the slab simulations and is shifted to colder simulations, with temperatures between 273 and 290 K.

The strength of the Hadley circulation is most strongly affected by ocean heat transport in the coldest simulations, with a steady decrease of the dynamical importance of ocean heat transport as the climate warms. For instance, the Hadley circulation in the ocean simulations is weaker than in the slab simulations by 58% in the coldest simulation, 37% in the reference simulation, but only by less than 1% in the warmest simulation. The difference in Hadley circulation strength between the ocean and slab simulations becomes small in the warmest climates because the Hadley circulations there are relatively weak and the meridional surface temperature gradients in the tropics and subtropics are small, so that the ocean heat transport (2.3) becomes inefficient. For example, in the warmest ocean simulation, the surface temperature contrast between the equator and the subtropical termini of the Hadley circulation amounts to only 4.5 K, compared with 8.0 K in the reference simulation. We expect the reduced importance of ocean heat transport in warm climates to be a general result, given the robustness of the mechanisms involved.

2.4.1.2 Eddy component and Rossby number

Theory. For the analysis of dynamical mechanisms responsible for these changes, it is helpful to decompose the Hadley circulation strength into a component associated with eddy momentum fluxes and a component associated with nonlinear mean momentum fluxes (Schneider and Bordoni, 2008). By vertical integration of the zonal momentum balance (2.1) over the upper branch of the Hadley circulation, from the top of the atmosphere to some pressure p_c above the top of the planetary boundary layer, it follows that the mass flux streamfunction $\Psi = \Psi_e(1 - \langle\mathrm{Ro}\rangle)^{-1}$ near the center of the Hadley cells can be decomposed into a component Ψ_e associated with eddy momentum fluxes and a bulk Rossby number $\langle\mathrm{Ro}\rangle$ associated with nonlinear mean momentum fluxes, with

$$\Psi(\phi, p) = -\frac{2\pi a \cos\varphi}{g} \int_0^p \overline{v}\, dp', \tag{2.7}$$

$$\Psi_e(\phi, p) = -\frac{2\pi a \cos\varphi}{fg} \int_0^p S_e\, dp', \tag{2.8}$$

where

$$S_e = \frac{1}{a\cos^2\varphi}\partial_\varphi(\overline{u'v'}\cos^2\varphi) + \partial_p(\overline{\omega' u'}), \tag{2.9}$$

and

$$\langle \mathrm{Ro} \rangle(\phi, p) = \frac{\Psi - \Psi_e}{\Psi}. \tag{2.10}$$

The bulk Rossby number $\langle \mathrm{Ro} \rangle$ is a nondimensional measure of the proximity of the Hadley circulation to the angular momentum–conserving limit, or of the relative importance of nonlinear mean momentum fluxes and eddy momentum fluxes in the zonal momentum balance. As for the local Rossby number, in the angular momentum–conserving limit, the eddy component Ψ_e vanishes so that $\langle \mathrm{Ro} \rangle \to 1$. In the eddy-driven limit, eddy momentum fluxes dominate, so that $\Psi \to \Psi_e$ and $\langle \mathrm{Ro} \rangle \to 0$. However, even $\langle \mathrm{Ro} \rangle \approx 1$ would not necessarily imply that all eddy fluxes are unimportant for the Hadley circulation, only that eddy momentum fluxes play a negligible role in the zonal momentum balance. Eddy energy fluxes may still influence the Hadley circulation through their effect on thermodynamic balances. We examine the behavior of the eddy component and the bulk Rossby number in both the slab and ocean simulations.

Bulk Rossby number $\langle \mathrm{Ro} \rangle$. The bulk Rossby number $\langle \mathrm{Ro} \rangle$, evaluated at the latitude ϕ_c of the streamfunction extremum and at the fixed level $\sigma_c = 0.7$, increases nearly monotonically with global-mean surface temperature: in simulations with (without) ocean heat transport, it increases from 0.18 (0.32) in the coldest climate, 0.41 (0.60) in the reference climate, to 0.86 (0.88) in the warmest climate (Fig. 2.5). Both slab and ocean simulations show a steady transition in the flow regime from low to large Rossby number as the climate warms, although the slab simulations have larger bulk Rossby numbers than the ocean

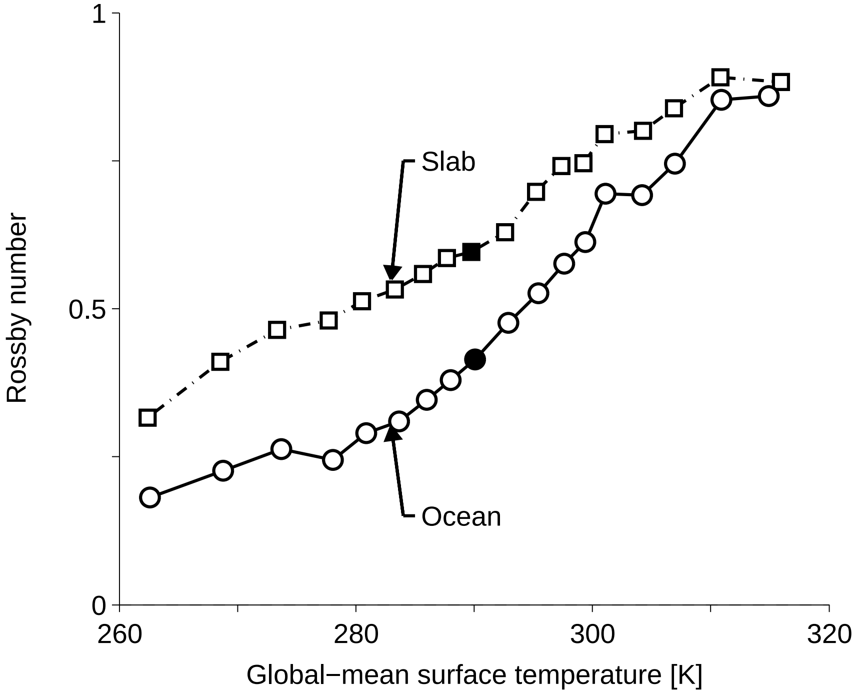

Figure 2.5: Bulk Rossby number in the simulations with (solid with circles) and without (dashed-dotted with squares) ocean heat transport. All quantities are evaluated at the latitude of the streamfunction extremum and at the level $\sigma_c = 0.7$, and are averaged over both hemispheres.

simulations, especially for cold climates (with $\alpha \leq 1.0$).

An increase in the bulk Rossby number implies an increase in the meridional shear of the zonal wind. The latter can be related to changes in the mean tropospheric zonal-wind shear and in the height of the tropopause. Our simulations indicate that in the deep tropics and near the center of the Hadley circulation, the bulk Rossby number increases primarily because the tropopause height increases. But the mean tropospheric zonal-wind shear in the subtropics also increases as the climate warms, and this likewise contributes to an increase in the bulk Rossby number there. The larger meridional shear of the zonal wind in the warm climates is consistent with a strengthening of the subtropical jet as the climate warms; the jet strengthens in simulations with (without) ocean heat transport from

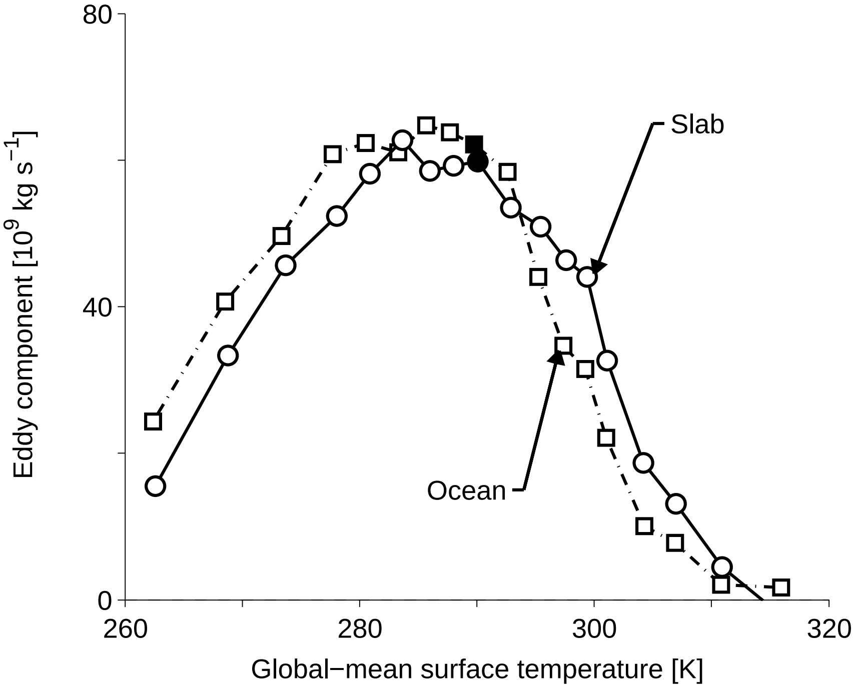

Figure 2.6: Eddy component of the mass flux streamfunction in the simulations with (solid with circles) and without (dashed-dotted with squares) ocean heat transport. All quantities are evaluated at the latitude of the streamfunction extremum and at the level $\sigma_c = 0.7$, and are averaged over both hemispheres.

$11\,\mathrm{m\,s^{-1}}$ ($15\,\mathrm{m\,s^{-1}}$) in the coldest climate, $29\,\mathrm{m\,s^{-1}}$ ($36\,\mathrm{m\,s^{-1}}$) in the reference climate, to $121\,\mathrm{m\,s^{-1}}$ ($125\,\mathrm{m\,s^{-1}}$) in the warmest climate (Fig. 2.3)—an indication of the reduced eddy damping of the zonal winds in the warm climates.

Eddy component Ψ_e. The eddy component Ψ_e, also evaluated at the latitude ϕ_c of the streamfunction extremum and at the fixed level $\sigma_c = 0.7$, changes nonmonotonically as the global-mean surface temperature increases (Fig. 2.6). It has nearly equal strength in the slab and in the ocean simulations. It is maximal near the same relatively cold climate regardless of ocean heat transport (ocean: $\alpha = 0.7$, global-mean surface temperature $\sim$284 K; slab: $\alpha = 0.8$, global-mean surface temperature $\sim$287 K), with nearly the same maximum values

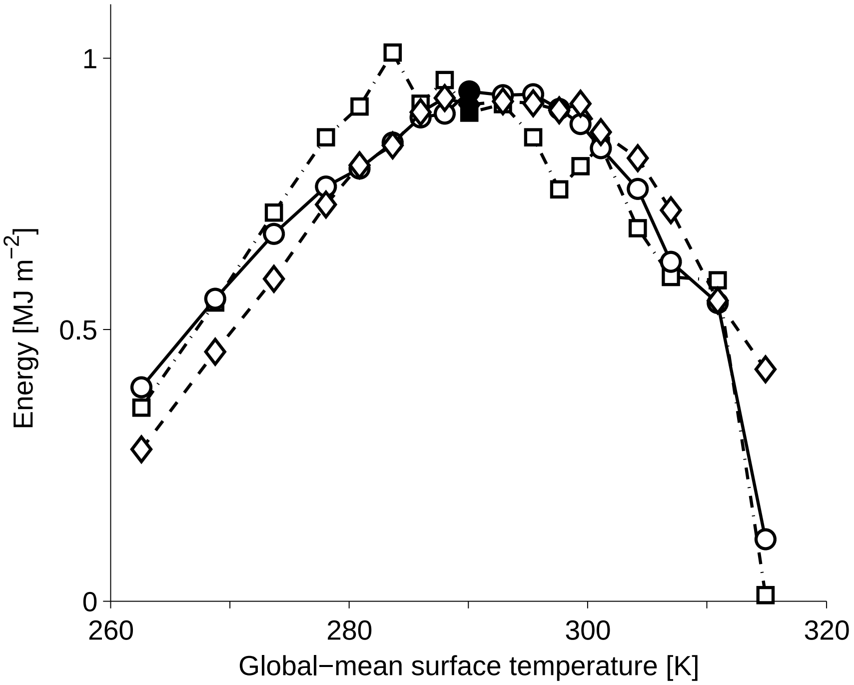

Figure 2.7: Mean available potential energy (dash-dotted with squares) and eddy kinetic energy (solid with circles) integrated over baroclinic zones, and globally integrated positively signed eddy momentum flux divergence (dashed with diamonds). Baroclinic zones are defined as the regions within 15° of the latitude of the maximum meridional heat flux at the level $\sigma = 0.84$. We computed MAPE using the same conventions as in O'Gorman and Schneider (2008a). Quantities are averaged over both hemispheres.

(∼$63\,\mathrm{Sv}$ and $65\,\mathrm{Sv}$). The relative importance of the eddy component in driving the Hadley circulation generally decreases as the climate warms, as already indicated by the local Rossby numbers (Fig. 2.2).

The nonmonotonic behavior of the eddy momentum flux divergence in the tropics, which is maximal near the reference simulation, is directly related to changes in eddy activity in the extratropics. Globally integrated, the eddy momentum flux divergence in tropical and polar regions equals the eddy momentum flux convergence in midlatitudes, where baroclinic instability preferentially occurs. Dimensional analysis suggests that the eddy momentum flux convergence scales like the product of the eddy kinetic energy and a characteristic inverse length scale (Schneider and Walker, 2008),

$$\langle \partial_y \overline{u'v'} \rangle \sim \frac{\langle \overline{u'^2} + \overline{v'^2} \rangle}{L_e}. \tag{2.11}$$

Here, $\langle \cdot \rangle$ is the average over a baroclinic zone. In our simulations, variations in eddy kinetic energy dominate variations in eddy length scales, so that the eddy kinetic energy and eddy momentum flux convergence vary linearly with each other (Fig. 2.7). In addition, the eddy kinetic energy scales with the mean available potential energy (MAPE), as shown in Fig. 2.7. The variations of the latter, in turn, can be decomposed into components associated with the meridional temperature gradient $\{\langle \partial_y \overline{T} \rangle\}$, inverse dry static stability $\{\Gamma\}$ ($\Gamma = -\kappa/p \, \langle \partial_p \overline{\theta} \rangle^{-1}$), thickness of the troposphere $\Delta p_t = p_s - p_t$, and the width of the baroclinic zone or eddy length scale L_e, as shown by O'Gorman and Schneider (2008a) for the slab simulations. Here, $\{\cdot\}$ is a vertical average over the troposphere in the baroclinic zone, p_s is surface pressure, and p_t tropopause pressure. Combining these terms gives

$$\langle \partial_y \overline{u'v'} \rangle \sim \Delta p_t \, \{\langle \partial_y \overline{T} \rangle\}^2 \{\Gamma\} L_e. \tag{2.12}$$

As shown by O'Gorman and Schneider for a warming climate in the slab simulations, the nonmonotonic behavior of the static stability, the steady increase in the thickness of the troposphere (tropopause height), and the decrease in the meridional temperature gradient all contribute to the nonmonotonic changes in MAPE, and thus to the nonmonotonic variations of the eddy component Ψ_e shown in Fig. 2.6. The same conclusions apply to the ocean simulations, as low-latitude ocean heat transport has only a minimal impact on the extratropical dynamics that control MAPE, and integrals of the eddy angular momentum flux divergence are nearly equal in the slab and ocean simulations. Nevertheless, in the warmest simulations with or without ocean heat transport, the eddy momentum flux divergence in the tropics differs significantly from the eddy momentum flux convergence in midlatitudes. This arises because a superrotating jet appears in the equatorial region, with associated eddy momentum flux convergence at the equator—likely caused by convectively generated Rossby waves, as in Schneider and Liu (2009)—which partially balances the eddy momentum divergence in the subtropics. A similar superrotating jet appears in the more comprehensive simulations of warm climates by Caballero and Huber (2010).

2.4.2 Hadley circulation extent

Several diagnostics have been used to define the subtropical terminus of the Hadley circulation. Reichler (2009) distinguishes two groups. The first comprises dynamical quantities, namely, (i) the latitude at which the mass flux streamfunction changes sign, (ii) the latitude at which the mean zonal surface wind changes from easterly to westerly, and (iii) the latitude of the subtropical jets. The second comprises derived quantities, namely, (iv) the poleward boundary of the subtropical arid zone, where precipitation balances evaporation in the zonal mean (Lu et al., 2007), (v) the poleward boundary of the tropical tropopause regime (Seidel and Randel, 2007), (vi) the poleward boundary of the tropical ozone regime (Hudson et al., 2006), and (vii) the poleward boundary of the tropical outgoing longwave radiation regime (Hu and Fu, 2007). On average, these diagnostics suggest that in the past

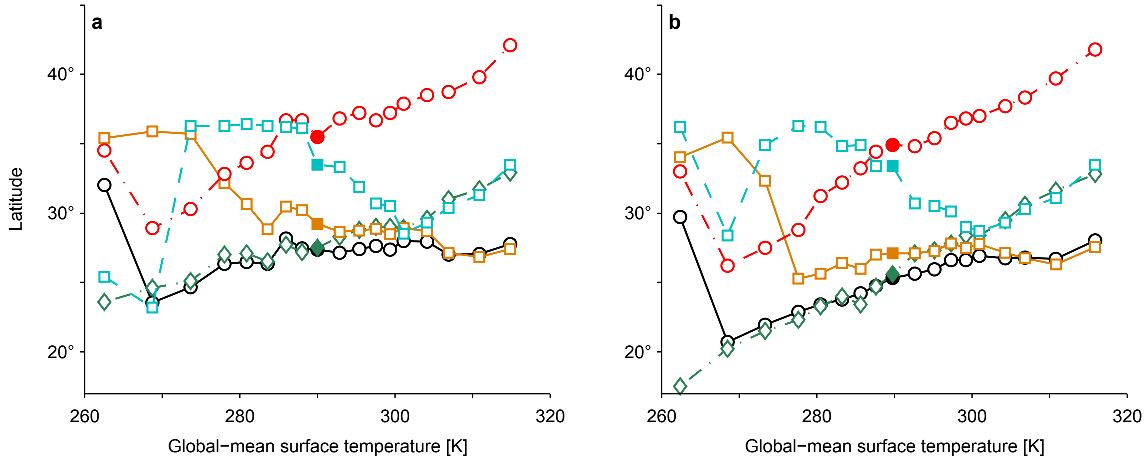

Figure 2.8: Extent of the Hadley circulation versus global-mean surface temperature. The extent is defined as the latitude where (i) the mass flux streamfunction at the level $\sigma_c = 0.7$ changes sign (solid black with circles), (ii) the mean zonal wind at the lowest level of the atmosphere vanishes (solid orange with squares), (iii) the mean zonal wind near the tropopause has a maximum (dash-dotted green with diamonds), (iv) mean evaporation equals precipitation (dash-dotted red with circles), (v) the tropopause rapidly changes height (dashed cyan with squares). Based on quantities averaged over both hemispheres. (a) Simulations with ocean heat transport. (b) Simulations without ocean heat transport.

30 years, the latitude band occupied by the Hadley circulation in the Northern and Southern Hemispheres together has widened at a rate of $\sim 1.4°$ per decade (Reichler, 2009). However, these trends exhibit large scatter; depending on the diagnostic and data source used, they vary between $\sim 0.3°$ per decade (Archer and Caldeira, 2008) and $3.0°$ per decade (Rosenlof, 2002; Seidel and Randel, 2007).

Additionally, these diagnostics do not necessarily change in lockstep as the climate changes, even if observational and modeling uncertainties were removed. The diagnostics are not simply related, and they are generally affected by different processes. Here we examine how the extent of the Hadley circulation changes in our simulations, comparing diagnostics (i)–(v), which are well-defined in the idealized GCM. We describe simulations with ocean heat transport (Fig. 2.8a), but the presence or absence of ocean heat transport

	Ocean simulations		Slab simulations	
Diagnostic	Latitude	Trend [K^{-1}]	Latitude	Trend [K^{-1}]
Ψ	27.4°	0.07°	25.3°	0.17°
u_s	29.2°	-0.14°	27.1°	0.11°
u_t	27.5°	0.08°	25.6°	0.26°
$\bar{P} = \bar{E}$	35.5°	0.22°	34.9°	0.35°
H_t	33.5°	-0.34°	33.4°	-0.33°

Table 2.1: Location of subtropical Hadley circulation terminus in reference simulation and trend (expansion rate) normalized by global-mean surface temperature increase. The expansion rates are averaged over 11 simulations centered on the reference simulations ($0.5 \leq \alpha \leq 2.0$). The terminus is determined according to different diagnostics: (i) zero of the mass flux streamfunction (Ψ); (ii) zero of the mean zonal surface wind (u_s); (iii) maximum of the mean zonal wind at the level of the midlatitude tropopause (u_t); (iv) latitude at which zonal-mean precipitation equals evaporation ($\bar{P} = \bar{E}$); (v) extremum of the meridional gradient of the tropopause height (H_t). The quantities are shown for the ocean and the slab simulations and are averaged over both hemispheres.

does not qualitatively affect the extent of the Hadley circulation or its rate of change with climate (compare Fig. 2.8a and 2.8b).

(i) The subtropical latitude at which the mass flux streamfunction is zero may be considered the most natural definition of the terminus of the Hadley circulation. This latitude varies with height, especially in the warmest simulations: for instance, Fig. 2.2 (bottom row) suggests that the poleward terminus is about $5°$ farther poleward near the tropopause than near the boundary layer top. Here we evaluate it at the level $\sigma_c = 0.7$ (as for other quantities before) because this fixed level is close to the level of the streamfunction extremum for all climates we simulated. The corresponding latitude generally shifts poleward as the climate warms, more rapidly in colder climates than in warmer climates (a prominent exception being the coldest simulation). However, the rate of expansion of the Hadley circulation according to this metric is modest. Averaged over the 11 simulations centered on the reference simulation

($0.5 \leq \alpha \leq 2.0$, global-mean surface temperatures between 281 and 301 K), the rate of expansion is only $0.07^\circ\,\mathrm{K}^{-1}$ relative to the global-mean surface temperature increase (Table 2.1). However, the results change qualitatively if in place of the latitude at which the streamfunction changes sign we use the latitude at which the absolute streamfunction value is below a low threshold value (e.g., $25\,\mathrm{Sv}$), or below a fraction of its extremal value (e.g., 20%). For instance, if we choose a $25\,\mathrm{Sv}$ threshold value, shown in Fig. 2.2 for 3 climates, the Hadley cells contract in the wamer simulations (with global-mean surface temperature greater than 299 K). Comparing changes in the terminus of the Hadley circulation obtained from the mass flux streamfunction therefore depends sensitively on how it is defined.

(ii) The latitude at which the mean zonal surface wind changes from easterlies in the tropics to westerlies in the extratropics shifts equatorward by about 6° between the coldest and the reference simulation; it remains near the zero of the mass flux streamfunction for climates warmer than the reference simulation. Near the reference simulation, the rate of expansion is $-0.14^\circ\,\mathrm{K}^{-1}$ relative to the global-mean surface temperature increase (Table 2.1).

(iii) The latitude of the subtropical jet, defined as the latitude at which the mean zonal wind at the level of the midlatitude tropopause is maximal, shifts poleward in a similar way as the zero of the mass flux streamfunction in simulations colder than the reference simulation; however, it shifts poleward more rapidly in warmer simulations. For all simulations except the coldest, the subtropical jet remains within 5° of the zero of the mass flux streamfunction. Near the reference simulation, the rate of expansion is $0.08^\circ\,\mathrm{K}^{-1}$ relative to the global-mean surface temperature increase (Table 2.1).

(iv) The latitude at which the zonal-mean precipitation equals evaporation, $\bar{P} = \bar{E}$, is generally located $\geq 8^\circ$ poleward of the zero of the mass flux streamfunction. It shifts poleward from 29° to 42° as the climate warms, implying a rate of expansion about 3 times as large as that obtained from the zero of the mass flux streamfunction (Table 2.1).

(v) The poleward boundary of the tropical tropopause regime is determined as the closest latitude to the equator at which the meridional gradient of the tropopause height has a local extremum. It shifts equatorward as the climate warms for simulations with global-mean surface temperature between 273 and 301 K, from 36° to 28°. This contraction is greater for simulations with global-mean surface temperatures between 288 and 301 K (Fig. 2.8a). However, it shifts poleward for warmer climates, in which it closely follows the location of the subtropical jet. Near the reference simulation, the rate of expansion is $-0.34^\circ\,\mathrm{K}^{-1}$ relative to the global-mean surface temperature increase (Table 2.1).

Hence, there are large differences in the subtropical terminus of the Hadley circulation and its shifts with climate according to the five diagnostics. Even the signs of the expansion rate can differ from diagnostic to diagnostic. Furthermore, the rate of expansion of the Hadley circulation according to the zero of the mass flux streamfunction—arguably the dynamically most relevant diagnostic—is considerably smaller than the rate of expansion according to the other diagnostics. Results from the slab simulations are similar (see

Fig. 2.8b for comparison), albeit with generally narrower Hadley circulations that expand poleward more rapidly as the climate warms (Table 2.1). The zero of the mass flux streamfunction is the diagnostic that is the most sensitive to the presence of ocean heat transport, as shown on Table 2.1, leading to expansion rates that differ by about a factor 3 between ocean and slab simulations near the reference simulations.

The rates of expansion of the Hadley circulation according to the diagnostics shown in Table 2.1 differ because they are controlled by different mechanisms. For example, the latitude at which zonal-mean precipitation equals evaporation depends strongly on the eddy fluxes of water vapor out of low latitudes into middle latitudes. However, these fluxes do not bear any simple relation to the zero of the mass flux streamfunction. In simulations with global-mean surface temperatures $\leq 288\,\mathrm{K}$, the zero of the mean zonal surface wind lies 2°–12° farther poleward of the zero of the mass flux streamfunction (Figs. 2.8a,b). In these colder simulations, the eddy momentum flux divergence at upper levels in the shallow troposphere and in the stratosphere extends poleward of the subtropical jet, between it and a midlatitude jet located 10°–30° poleward (see, e.g., Fig. 2.2, top row). Because the vertically integrated eddy momentum flux divergence at these latitudes (where the local Rossby number is small) balances the drag on the mean zonal surface wind, surface easterlies extend poleward of the zero of the mass flux streamfunction in the troposphere. As the climate warms, the eddy momentum flux divergence in the midlatitude stratosphere weakens, and the zero of the mean zonal surface wind moves closer to the zero of the mass flux streamfunction.

Simulations of global warming scenarios with comprehensive GCMs suggest that the zero of the mass flux streamfunction shifts poleward at rates of about 0.5° per 1 K global-mean surface temperature increase (Lu et al., 2007). Idealized GCMs forced by varying sea surface temperatures (SSTs) suggest that the zero of the mass flux streamfunction shifts poleward at rates of about 0.2° to 0.25° per 1 K global-mean surface temperature increase (Frierson et al., 2007). This is similar to the expansion rate ($0.17^\circ\,\mathrm{K}^{-1}$) in our slab simulations near the reference climate (Table 2.1), and up to $\sim$3 times greater than the expansion rate ($0.07^\circ\,\mathrm{K}^{-1}$) in our ocean simulations. The discrepancies between the rate of expansion of the Hadley circulation in comprehensive and idealized GCMs may be due to the presence of continents as well as of a seasonal cycle.

2.4.3 Energy transport

The strength of the Hadley circulation may also be measured in terms of how much energy it transports meridionally. If one neglects the small transport of kinetic energy, the total energy transport in the atmosphere is equal to the transport of moist static energy $s = s_d + Lq$, which consists of contributions from the dry static energy $s_d = c_pT + gz$ and from the latent heat Lq (symbols have their conventional meaning; see, e.g., Peixoto and Oort 1992, chapter 13). The Hadley circulation transports dry static energy poleward (because the dry static energy in the upper branch is higher than that in the lower branch), and it transports latent heat equatorward (because the specific humidity in the lower branch

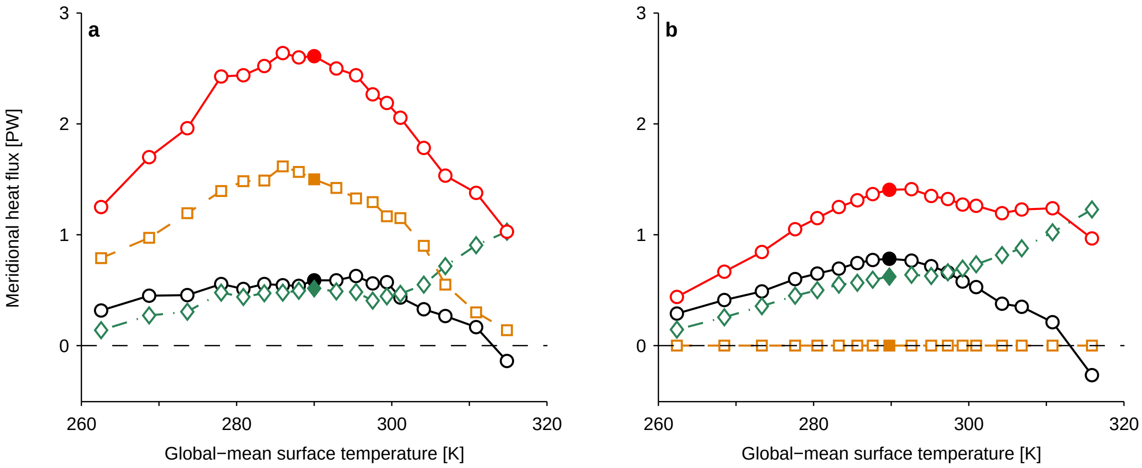

Figure 2.9: Vertically integrated heat fluxes evaluated at the center of the Hadley cells (latitude of the streamfunction extremum). Total ocean-atmosphere heat flux (red solid with circles) and its components: mean component (black solid with circles) and eddy component (green dashed-dotted with diamonds) of the moist static energy flux; ocean heat flux (orange dashed with squares). The fluxes are averaged over both hemispheres. (a) Simulations with ocean heat transport. (b) Simulations without ocean heat transport.

is greater than that in the upper branch). The net transport of moist static energy is the residual of these partially compensating fluxes, and it is generally much smaller than the fluxes individually.

The moist static energy flux associated with the Hadley circulation (its mean component) in the ocean simulations is shown in Fig. 2.9a, along with the eddy flux of moist static energy (its eddy component) and the ocean heat flux, all evaluated at the center of the Hadley cells. The eddy component of the moist static energy flux is comparable with the mean component over a wide range of climates, although the eddy components of the dry static energy and latent heat fluxes individually are considerably smaller than the mean components: while the mean components of the dry static energy and latent heat fluxes partially compensate, the eddy fluxes of both dry static energy and latent heat are directed poleward (downgradient). Both the mean and the eddy components of the moist static energy flux strengthen as the climate warms for simulations with global-mean surface temperatures below 300 K. For simulations with global-mean surface temperature above 300 K, the mean component weakens sharply and even becomes negative in the warmest simulations, while the eddy component continues to increase essentially monotonically. The sum of the ocean heat flux and the atmospheric moist static energy flux at the center of the Hadley cells, the total atmosphere-ocean heat flux, peaks near the reference simulation (Fig. 2.9a). Over the wide range of climate we simulated, the partition between the mean component of the moist static energy flux and the ocean heat transport remains nearly unchanged; its value, which varies between $\sim 25\%$ and $\sim 40\%$, is in good agreement with the prediction of Held (2001). The changes with climate of the total heat flux resemble those of the mass flux streamfunction (compare Figs. 2.4 and 2.9a), primarily because the ocean heat flux dominates the total heat flux, and its strength is tightly coupled to the strength of the Hadley circulation.

The moist static energy flux in the slab simulations behaves similarly to that in the ocean simulations (compare Figs. 2.9a and 2.9b). However, both the mean and eddy components are up to $\sim 60\%$ larger in the slab simulations than in the ocean simulations. But even the larger moist static energy fluxes in the slab simulations do not compensate for the lack of ocean heat transport. For instance, at the reference simulations, the total heat transport is 40% smaller in the slab simulations. This contrasts with the heat fluxes at the subtropical termini of the Hadley circulation, which are less sensitive to ocean heat transport. For instance, the difference between the moist static energy fluxes in the slab and ocean reference simulations at the center of the Hadley circulation is 0.45 PW, which is significantly larger than the corresponding difference at the termini of the Hadley circulation (only 0.10 PW). It implies that most of the additional heat carried by the atmosphere-ocean system in the ocean simulations is radiated to space in the subtropics.[2]

Overall, it is clear that also if measured in terms of how much energy it transports meridionally, the strength of the Hadley circulation can change nonmonotonically with global-mean surface temperature. The fact that the energy transport by the Hadley circulation (though not by the total circulation including eddies) can become negative (equatorward) illustrates some of the difficulties that can arise in devising theories for how the mass flux in the Hadley circulation relates to the energy flux.

2.5 Conclusion

We have introduced an idealized GCM with a one-dimensional representation of ocean heat transport that is dynamically coupled to the surface wind stress. With this idealized GCM, we have simulated a wide range of climates by varying the optical thickness of a longwave absorber, comparing the simulations with ocean heat transport with otherwise identical previous simulations without ocean heat transport (O'Gorman and Schneider, 2008b). Because the ocean heat transport dominates the total ocean-atmosphere heat transport in low latitudes, it affects the dynamics of the tropical atmosphere. It is necessary to represent ocean heat transport in idealized GCMs to obtain Hadley circulations in a dynamical

---

[2] These results contradict the hypothesis of Trenberth and Stepaniak (2003), according to which extratropical eddy heat fluxes were posited as a driver of the Hadley circulation. In our simulations, changes in the strength of the Hadley circulation between ocean simulations and slab simulations are not accompanied by changes in extratropical eddy heat fluxes that are nearly as large, and the total heat flux is not necessarily "seamless" in the subtropics.

regime similar to Earth's, with relatively low Rossby numbers at the center of the equinox or annual-mean Hadley circulation. Our principal results were as follows:

1. Ocean heat transport strongly influences the Hadley circulation in climates resembling present-day Earth's and colder. Its influence diminishes as the climate warms and meridional temperature gradients in low latitudes are reduced.

2. As the climate warms, the Hadley circulation strengthens in colder simulations but weakens in warmer simulations. In the coldest/warmest simulations, it is $\sim$70% weaker than in the reference simulations with or without ocean heat transport.

3. As the climate warms, the bulk Rossby number at the center of the Hadley circulation increases from 0.2 in the coldest ocean simulations and 0.3 in the coldest slab simulations to ~ 1 in the warmest simulations: The coldest simulations are strongly influenced by eddy momentum fluxes but the warmest simulations are closer to being angular momentum conserving. Eddy momentum fluxes influence the Hadley circulation more strongly in simulations with ocean heat transport than in simulations without ocean heat transport.

4. In simulations with climates resembling present-day Earth's and colder, the Hadley circulation strength scales with the low-latitude divergence of eddy momentum fluxes. The latter in turn scales with the midlatitude mean available potential energy. Thus, midlatitude conditions influence the strength of the tropical circulation.

5. The Hadley circulation widens by $\sim 5^\circ$ latitude between the coldest and warmest simulations. The widening rate is greater in climates resembling present-day Earth's

and colder. However, different diagnostics for the extent of the Hadley circulation change with climate in different ways because they are often not dynamically related.

Some of our results—such as the behavior of the Hadley circulation strength—may be modified if additional processes (e.g., a seasonal insolation) and feedbacks (e.g., ice-albedo feedback) are taken into account. Nevertheless, the non-monotonicity of numerous key variables already in our relatively simple setting and the intermediate values of the bulk Rossby number suggest that an accurate prediction for the changes of the large-scale tropical dynamics with climate requires understanding both the changes in the Rossby number and in eddy fluxes. Devising a theory that takes both effects into account remains as a challenge.

2.6 Acknowledgments

We thank Paul O'Gorman for performing the simulations without ocean heat transport and for helpful comments and discussions. We are grateful for support by the National Science Foundation (Grants ATM-0450059 and AGS-1019211), the Davidow Discovery Fund, and a David and Lucile Packard Fellowship. The simulations were performed on the Division of Geological and Planetary Sciences's Dell cluster at the California Institute of Technology. The program code for the simulations described in this chapter, and the simulation results themselves, are available from the authors upon request.

Chapter 3

The Influence of Moist Baroclinic Waves on the Termination of the Hadley Circulation: an Idealized GCM Study

3.1 Introduction

Observational studies suggest that the mean meridional overturning circulation in the tropics has widened the past 30 years (Hu and Fu, 2007; Seidel and Randel, 2007; Seidel et al., 2008). This widening has been qualitatively reproduced in general circulation model (GCM) simulations of a warming climate, in which it is also accompanied by a poleward shift of the subtropical dry zones (Lu et al., 2007). Nonetheless, although GCM simulations and observations are consistent in the sign of the widening trend, the magnitudes of the simulated trends can differ from the observations by up to a factor 10 (Johanson and Fu, 2009).

Determining the causes of the model differences is difficult because there is no convincing theoretical account of how the widening of the Hadley circulation relates to other climatic variables. A theory that accounts for the width of the Hadley circulation across a range of climates is lacking (Schneider, 2006; Schneider et al., 2010). Comprehensive

GCM studies (with an active hydrologic cycle) indicate that the widening of the Hadley circulation under global warming may be caused by a poleward shift in baroclinic wave activity (Lu et al., 2007; Frierson et al., 2007; Kang and Lu, 2012). Yet the conclusions of these studies are limited in scope because the complexity of the GCMs used and the limited amplitude of the climate change signals analyzed effectively preclude an in-depth quantitive comparison with theory.

On the other hand, progress has been made using dry idealized GCMs without an active hydrology. There, a criterion for the strength of baroclinic wave activity captures the shifts in the terminus of the Hadley circulation over a wide range of climates (Korty and Schneider, 2008). But it is unclear whether this may be applied to climates that have an active hydrologic cycle such as Earth's (Schneider and O'Gorman, 2008; Schneider et al., 2010; O'Gorman, 2010).

Here we use an idealized moist GCM with an active hydrologic cycle to investigate changes in the terminus of the Hadley circulation over a wide range of climates. We show that the terminus of the Hadley circulation and its poleward shift under global warming can be accounted for by a generalized form of the criterion for the strength of baroclinic wave activity that was proposed in studies of dry atmospheric circulations.

3.2 Theory

Changes in the width of the Hadley circulation have been described by a hierarchy of theories, which consider the existence of an overturning circulation in the low-latitudes resulting from a latitudinal contrast in both the near-surface heating and the Coriolis acceleration;

this circulation, by carrying heat poleward, effectively reduces the extreme meridional thermal imbalance found in a radiative-convective equilibrium. The simplest dynamical regime for the Hadley circulation is an axisymmetric overturning circulation extending to a finite latitude, beyond which radiative–convective equilibrium prevails (Schneider, 1977; Held and Hou, 1980). Axisymmetric flow were not originally viewed as accounting for the behavior of Earth's Hadley circulation, however, but as providing a basic state for studies of baroclinic instability (e.g., Schneider, 1977): in this regime, the zonal wind speeds would be large enough in the subtropics to be linearly unstable to baroclinic instability (e.g., Phillips, 1954). This has led to the notion that the axisymmetric Hadley circulation may extend only to the latitude where baroclinic instability "sets in" (Held, 2000).

3.2.1 Supercriticality: theory

The quasigeostrophic two-layer model shows that a mean flow becomes linearly unstable to baroclinic instability whenever the zonal wind shear exceeds a critical threshold, i.e., whenever the shear becomes supercritical to the most unstable mode (Phillips, 1954):

$$\partial_z u = \frac{\beta r_d \Delta_v \theta}{f^2 H_o}. \tag{3.1}$$

Here, f is the planetary vorticity, β the planetary vorticity gradient, r_d the gas constant for dry air, $\Delta_v \theta$ the potential temperature contrast between the top and the bottom layers of the two-layer model, and H_o the scale height defining the vertical coordinate,

$$Z = -H_o \log \frac{p}{p_{srf}}, \tag{3.2}$$

where p_{srf} is the pressure at the surface. Using observational data, Stone (1978) found the zonal wind profile in Earth's atmosphere was consistent with the vertical shear being nearly equal to the critical profile predicted by Eqn. 3.1, in regions of large synoptic activity. However, this critical shear for baroclinic instability was shown to be an artifact of the crude vertical discretization in the two-layer model (e.g., Held, 1982); In addition, the quasigeostrophic framework does not allow baroclinic waves to modify the thermal stratification of their environment, and thus might not be applicable to a fully nonlinear flow (e.g., Schneider, 2004).

The success of Eqn. 3.1 in predicting the zonal wind profile on Earth may be ascribed to its geometric interpretation as a depth over which baroclinic eddies extend (cf. Held, 1978). In particular, Schneider and Walker (2006) derived a non-dimensional criterion, called supercriticality (Sc), which quantifies the ratio of the depth scale of baroclinic entropy fluxes to the height of the tropopause:

$$S_c = \frac{\Delta_h \theta}{\Delta_v \theta} \approx \frac{\bar{p}_{srf} - \bar{p}_e}{\bar{p}_{srf} - \bar{p}_t}. \tag{3.3}$$

Here, $\overline{(.)}$ defines a temporal and zonal mean; $\bar{p}_{srf}$ is the mean surface pressure, $\bar{p}_t$ is the mean depth of the troposphere, and $\bar{p}_e$ is the mean depth to which baroclinic eddy vertical entropy fluxes propagate; $\Delta_h \theta$ is the meridional temperature contrast (a measure of the near-surface zonal wind shear with units of a meridional potential temperature difference) and $\Delta_v \theta$ is the static stability contrast (a measure of the near-surface static stability with units of a vertical potential temperature difference), which were defined as follows:

$$\Delta_h \theta = -\frac{f}{\beta} \partial_y \overline{\theta}_s, \tag{3.4}$$

and

$$\Delta_v \theta = -2\, \partial_p \bar{\theta}_s \, (\bar{p}_{srf} - \bar{p}_t). \tag{3.5}$$

Here, we define $(.)_s$ as a vertical average from the 800 to 700 hPa pressure levels, which represents a tropospheric layer located just above the planetary boundary layer; $-\partial_p \bar{\theta}_s$ is the near-surface static stability and $\partial_y \overline{\theta}_s$ the near-surface meridional gradient of the mean potential temperature. Supercriticality was obtained by assuming the thermal stratification to be controlled by geostrophic eddy fluxes, which diffuse potential vorticity adiabatically above the boundary layer and entropy within the boundary layer. Supercriticality becomes equivalent to the two-layer model critical shear (Eqn. 3.1) whenever $S_c \sim 1$; however, unlike the former, supercriticality is not a linear instability criterion and thus does not quantify the stability of the mean flow to linear baroclinic instability.

3.2.2 A bulk estimate for supercriticality

Supercriticality may be evaluated either locally (Eqn. 3.3) or as a bulk average. Schneider and Walker (2006) argued that supercriticality should be estimated over a region corresponding to the size of the largest baroclinic eddies. Indeed, eddy diffusion of potential vorticity and near-surface entropy by baroclinic geostrophic eddies occur primarily on the lengthscale of the most energetic eddies, whose size may be estimated from the extent of regions of strong eddy heat fluxes; following Schneider and Walker (2006), we define the baroclinic zones as regions where the near-surface eddy meridional temperature flux profile is greater than 70% of its maximum value, whose location at latitude φ_M defines the center of the storm tracks. On Earth-like planets (in size and rotation rate), this region covers most of the extratropics, consistent with the deformation radius being of the scale of the planet. We thus define a bulk estimate of supercriticality,

$$\langle S_c \rangle = \frac{\langle \Delta_h \theta \rangle}{\langle \Delta_v \theta \rangle}, \tag{3.6}$$

where $\langle \Delta_h \theta \rangle$ is defined as the bulk meridional temperature contrast,

$$\langle \Delta_h \theta \rangle = \frac{f(\varphi_M)}{\beta(\varphi_M)} \left[\partial_y \overline{\theta}_s \right], \tag{3.7}$$

and $\langle \Delta_v \theta \rangle$ as the bulk static stability contrast:

$$\langle \Delta_v \theta \rangle = -2 \left[\partial_p \overline{\theta}_s \right] \left[\overline{p}_{srf} - \overline{p}_t \right]. \tag{3.8}$$

Here, $\langle (.) \rangle$ indicates a bulk estimate, and $[(.)]$ defines a meridional average over the baroclinic zone. Similarly to its local estimate shown in Eqn. 3.3, bulk supercriticality characterizes whether baroclinic waves control the thermal stratification: hence, $\langle S_c \rangle \sim 1$ if baroclinic entropy fluxes extend to the tropopause, and $\langle S_c \rangle \leq 1$ if the tropopause height is set by other processes and baroclinic entropy fluxes are shallower. This bulk estimate of supercriticality, by accounting for transport and mixing on the largest eddy sizes, is the most robust definition of the criterion for charactering the efficiency of baroclinic waves in controlling the height of the tropopause.

Using the idealized dry GCM described in section 3.3.1, Schneider and Walker (2006) found that bulk supercriticality generally achieved $\mathcal{O}(1)$ values over a wide range of thermal parameters, implying that baroclinic waves control the depth of the troposphere in these climates.

3.2.3 Evaluating the terminus of the Hadley cell from supercriticality

These results suggest using supercriticality to locate the terminus of the Hadley circulation in climates in which baroclinic eddies influence the Hadley circulation. Using S_c as a local-in-latitude measure of the depth of baroclinic entropy fluxes, Korty and Schneider (2008) hypothesized that the Hadley circulation extends to the latitude at which S_c first exceeds a critical $\mathcal{O}(1)$ value (S_c generally increases with latitude because the geometric term increases rapidly with latitude). This is borne out of the mean zonal momentum balance,

$$f(1 - \mathrm{Ro})\overline{v} \approx S_e, \tag{3.9}$$

when evaluated at the Hadley circulation terminus. Here, v is the meridional velocity, and Se the eddy momentum flux divergence. This relation neglects the vertical advection of mean zonal momentum by the mean vertical flow. The local Rossby number $\mathrm{Ro} = -\overline{\xi}/f$, with relative vorticity ξ, quantifies the relative importance of eddy momentum fluxes in driving the Hadley circulation (Walker and Schneider, 2006; Schneider, 2006; Levine and Schneider, 2011). The axisymmetric regime corresponds to the limit $\mathrm{Ro} \to 1$, in which the upper branch of the Hadley circulation is controlled by diabatic heating and eddy heat fluxes but otherwise is unaffected by eddy momentum fluxes (Schneider, 1977; Held and Hou, 1980). The other limit $\mathrm{Ro} \to 0$ corresponds to eddy momentum fluxes solely controlling the mean overturning circulation, with no direct control by diabatic or eddy heat fluxes (e.g., Dickinson, 1971).

At the center of the Hadley cells, Rossby numbers are less than 0.5 on Earth in the annual mean. Our understanding of the Hadley circulation in this intermediate range of Rossby numbers is poor: there, the combination of eddy fluxes with the nonlinearity of the momentum balance has prevented analytical progress. At the terminus, on the other hand, the Rossby number is typically much smaller than 1. In this regime, a reversal in the sign of the eddy momentum flux convergence (Se) implies locally a change in the direction of the mean meridional flow (see Eqn. 3.9 setting Ro to 0). Poleward of the latitude of the mean meridional flow reversal, convergence of meridional eddy momentum fluxes near the tropopause implies a local divergence of meridional wave activity fluxes, consistent with baroclinic entropy fluxes reaching the tropopause. This provides a mean to evaluate the terminus of the Hadley circulation by evaluating the latitude where baroclinic eddies start reaching the tropopause height, i.e., where $S_c \sim 1$ just starts to be achieved locally.

Using the same set of simulations as Schneider and Walker (2006), Korty and Schneider (2008) showed that supercriticality at the Hadley circulation terminus achieved a nearly constant value, in climate scenarios with moderate to strong thermal forcings; this value was found to be somewhat smaller than its bulk estimate over the baroclinic zones, consistent with the terminus defining a boundary for convergence of wave activity.

3.2.4 Effective static stability

Schneider and Walker (2006) obtained Eqn. 3.3 by neglecting all diabatic sources and sinks, assuming those to be small compared to the instantaneous heating tendency set by baroclinic geostrophic eddy entropy fluxes; this is borne out of the radiative cooling timescale of the atmosphere, which is significantly longer than that of a baroclinic wave lifecycle. Yet, other processes can affect the thermodynamic budget on timescales similar to or shorter than that of a baroclinic wave lifecycle: in particular, condensation in convective and stratiform clouds are know to affect the intensity and structure of baroclinic waves (e.g., Lapeyre and Held, 2004). Condensation in convective and stratiform clouds is controlled by different processes, and occur on different timescales and lengthscales: while convective events arises from an unstable static stability and may last for a few hours over a region only a few tens of kilometer wide, stratiform clouds are controlled by the quasi-horizontal flux of water vapor by baroclinic eddies and can cover regions several hundred kilometers wide. Condensation, either in stratiform or convective clouds, can strongly affect the efficiency of heat transport in baroclinic waves and thus their ability to control the depth of the troposphere.

Using the idealized moist GCM described in section 3.3.2, Schneider and O'Gorman (2008) found a considerable effect of moisture on the scaling shown in Eqn. 3.3: in particular, bulk supercriticality was observed to decrease as global climate warms, in contrast to its near-invariance in the dry GCM simulations shown in Schneider and Walker (2006). Only in the coldest moist simulations were $\mathcal{O}(1)$ values of supercriticality observed. Schneider and O'Gorman (2008) attributed this decrease with global warming to a concomitant increase in the static stability and tropopause height, hinting at the need for a modified form of bulk static stability contrast ($\langle \Delta_v \theta \rangle$), which would account for the effect of moisture on baroclinic waves.

To devise a theory for a modified static stability (hereafter called effective stability), one needs to address the dynamically coupled nonlinearity that condensation introduces in the thermodynamic budget. In moist atmospheres, updrafts are associated with saturation and concomitant latent heat release; in downdrafts, however, this does not occur. Following O'Gorman (2010), this asymmetry between updrafts and downdrafts in baroclinic waves may be incorporated in the entropy budget as follows:

$$\partial_t \theta + ... + w \partial_p \theta = ... + Q_c \mathcal{H}(-w). \tag{3.10}$$

Here, Q_c refers to diabatic heating associated with phase change, and $\mathcal{H}(-w)$ is the Heaviside function selectively removing downdrafts. Not shown in Eqn. 3.10 are horizontal advective fluxes as well as any other diabatic heating sources not explicitly associated with this dynamical nonlinearity (e.g., radiative fluxes). An expression for the phase change heating term (Q_c) can be easily obtained by assuming it to be completely balanced by local vertical advective cooling:

$$Q_c = w^{\uparrow} \partial_p \theta^{\uparrow}. \tag{3.11}$$

Here, $(.)^{\uparrow}$ defines updraft regions. To determine the static stability in updraft regions, we consider the coupling of convective and stratiform precipitation in cyclonic updrafts.

Both forms of precipitation generally occur around the cyclonic core of a baroclinic wave: there, large-scale upwelling promotes stratiform precipitation but also destabilize the air column locally, leading to convective precipitation in the cyclonic core (Ralph et al., 2004). Convective precipitation may occur as well in the sharp fronts separating subtropical and polar air masses around the cyclonic core (e.g., Emanuel, 1985). The interdependency of convection and stratiform precipitation suggests that the static stability in regions of large-scale updrafts may be near its local convective lapse rate, i.e.,

$$\partial_p \theta^{\uparrow} = \partial_p \theta \mid_{\theta^*_{srf}} . \tag{3.12}$$

Here, $\partial_p \theta^{\uparrow}$ is the static stability set by air parcels lifted pseudo-adiabatically from the surface and thus conserving their near-surface moist entropy (θ^*_{srf}). Consistent with these approximations, a linearized version of the local entropy budget is derived as follows:

$$\partial_t \theta' = -w' \, \partial_p \overline{\theta} + w^{\uparrow'} \, \overline{\partial_p \theta \mid_{\theta^*_{srf}}}. \tag{3.13}$$

This linearized budget differs from that shown in O'Gorman (2010) in its formulation for static stability in updraft regions: in this study, static stability in updrafts regions is set by the near-surface moist entropy, while in O'Gorman (2010) it is set by the local saturated moist entropy. While our formulation is valid only in scenarios where convection sets the thermal stratification in cyclonic updrafts, that of O'Gorman (2010) does not require stratiform precipitation to be tied to convective precipitation there.

Similarly to O'Gorman (2010), the eddy upward velocity is posited to depend linearly on the eddy vertical velocity itself:

$$w^{\uparrow'} = \lambda w' + \epsilon. \tag{3.14}$$

Here, ϵ is a small residual and λ a rescaling factor. The value of this factor λ is set by the instantaneous eddy vertical velocity latitudinal distribution; it depends not only on its variance but may also be sensitive to higher order statistics (in particular its skewness). For a binary distribution, however, the factor λ is simply proportional to the area occupied by downdrafts regions; there, its value converges to 0, when updrafts nearly covers the entire domain, and to 1, when these only cover a very small surface area, respectively. This relation to updraft surface area remains approximately true even for non-binary distributions such that found in Earth's atmosphere: in the deep tropics, where updrafts are confined to a small part of the domain, NCEP-2 reanalysis shows that λ converges to 1, while its value is near 0.5 in the extratropics, the latter being consistent with updraft and downdraft regions being nearly equal in size there (O'Gorman, 2010). Asymmetry between updrafts and downdraft area coverage arises from a dynamical nonlinearity, such as the coupling of updrafts with water vapor condensation; in dry atmospheres, on the other hand, lack of diabatic heat sources tied to updrafts leads to an equipartition between updrafts and downdrafts. The factor λ, which quantifies primarily the effect of phase change on the geometry of the baroclinic waves, is combined to Eqn. 3.13 to provide an expression for the effective static stability felt by baroclinic waves, averaged over many lifecycles:

$$\overline{\partial_p \theta^{\text{eff}}} = \partial_p \overline{\theta} - \lambda\, \overline{\partial_p \theta \,|_{\theta^*_{srf}}}. \tag{3.15}$$

Here, $\partial_p\theta^{\text{eff}}$ is defined as the effective static stability. O'Gorman (2010) showed the extratropical values of λ to be near 0.5, both in present day climate and over a wide range of climates. Setting the factor λ to 0.5, we define an effective static stability contrast, similar to Eqn. 3.8,

$$\Delta_v^{\text{eff}} = -2\,\overline{\partial_p\theta_s^{\text{eff}}}\,(\bar{p}_{srf} - \bar{p}_t), \tag{3.16}$$

and a bulk effective static stability contrast,

$$\left\langle \Delta_v^{\text{eff}}\theta \right\rangle = -2\,\left[\overline{\partial_p\theta_s^{\text{eff}}}\right]\,\left[(\bar{p}_{srf} - \bar{p}_t)\right], \tag{3.17}$$

which were used to define a local and a bulk effective supercriticality respectively.

O'Gorman (2010) found his version of the bulk effective supercriticality to be more invariant with global warming than the classical form; also, a constant value for effective supercriticality was found to properly diagnose the terminus of the Hadley circulation over a wide range of global warming scenarios. Yet, questions about the validity of this effective criterion remain: For instance, O'Gorman (2010) found its value to be systematically larger than in the classical form, even in the coldest climates where both forms ought to converge. In addition, this effective stability was tested for only a limited set of climates, which were all run at the same insolation contrast value. Yet, Schneider and Walker (2006) and Korty and Schneider (2008) found that the classical form of supercriticality applies best to scenarios forced by large thermal forcing contrasts, which calls for testing supercriticality not only in global warming scenarios but also in scenarios with different insolation contrasts.

3.3 Idealized GCM

3.3.1 Dry idealized GCM

A complete description of the idealized dry GCM may be found in Schneider and Walker (2008). The planet is bounded by a spatially uniform and thermally insulating surface. A spectral dynamical core solves for the horizontal large-scale motions in the atmosphere with a resolution of T42 in all experiments. Vertical motion is solved on a discretized grid of 30 vertical sigma levels. Momentum and dry entropy fluxes from the surface to the top of the boundary layer are parameterized by a Monin-Obhukov diffusive scheme; Frictional dissipation at the surface is parameterized by a bulk aerodynamic formula. Heating sources and sinks are represented by a simple Newtonian relaxation of potential temperatures toward a zonally symmetric radiative equilibrium profile. The potential temperature profile in radiative equilibrium has a quadratic profile at the surface and a prescribed static stability that is unstable to dry convection. The relaxation timescale has a zonally symmetric profile that varies with latitude and height from 7 days near the surface to 50 days in the interior atmosphere (Schneider, 2004). Convection is parameterized by a quasi-equilibrium convection scheme. The convective lapse rate is varied by rescaling the dry adiabatic lapse rate by a factor γ less than or equal to 1. This model neglects the thermodynamic effects of phase change for water except for its effect on convection. By representing the latter process by a variable convective lapse rate, the static stability in convective regions can be varied in a way analogous to that resulting from a change in the near-surface moisture content in a moist atmosphere. Hence, decreasing the rescaling factor γ is analogous to increasing the moisture content just above surface.

A large range of climate is simulated by varying the pole-to-equator temperature contrast $\Delta_h \theta_s^e$ from 15 to 300 K and the convective lapse rate rescaling factor γ from 0.6 to 1.0. All 80 simulations were run for 2000 days and their statistics computed from an average over the last 600 days, sampled 4 times daily, after a statistically steady state has been reached.

3.3.2 Moist idealized GCM

The idealized moist GCM is extensively described in O'Gorman and Schneider (2008b). The planet is covered by a uniform ocean with a thermal inertia of one meter of water and an albedo of 0.38. Other constants (insolation, rotation rate, gravity, etc.) are kept the same as on Earth. A spectral dynamical core solves for the horizontal large-scale motions in the atmosphere with a resolution of T42 in all experiments; A higher resolution (T85) was also used for a set of simulations describing a reference global warming scenario, to test the robustness of our results to changes in the numerical resolution. Vertical motion is solved on a discretized grid of 30 vertical sigma levels. Water vapor is advected by the dynamical core and may condense whenever saturation occurs on the grid scale. Momentum, moisture and dry entropy fluxes from the surface to the top of the boundary layer are parameterized by bulk aerodynamic formulas and a Monin-Obhukov diffusive scheme. Moist convection is parameterized by a quasi-equilibrium convection scheme (Frierson, 2007; Frierson et al., 2006). Radiative heating rates are computed for a gray atmosphere with no clouds, in which the longwave optical thickness accounts for longwave absorption by water vapor and well-mixed greenhouse gases. The GCM is forced by a quadratic representation of insolation at the top of the atmosphere. This insolation is steady, i.e., there is no diurnal or seasonal cycle. The default insolation profile is a close approximation to Earth's in the annual mean. The reference longwave optical thickness produces a climate resembling Earth's climate in the annual mean when combined with an idealized representation for ocean heat transport (Levine and Schneider, 2011).

To simulate a large range of climates, we vary the longwave optical depth and the insolation profile in climate scenarios both with and without simple ocean heat transport (ocean simulations are described in appendix 3.7.2). The reference profile for the longwave optical depth is rescaled to mimic variations in greenhouse gas concentrations; we use 7 different rescaling factors ranging from 0.2 to 4.0. The insolation profile is varied in a way that conserves its global value; We use between 14 and 19 insolation contrast values for every optical depth value, for a total of 109 climates with a dynamically coupled ocean heat transport, and 109 climates without a dynamically coupled ocean heat transport. Some of these insolation contrast values are so large that insolation becomes negative at the poles; these simulations, despite not being realistic planetary configurations, extends our study to the same climate range as the dry GCM simulations. All simulations were run for 9 years and their statistics computed from an average over the last 4 years, sampled 4 times daily, after a statistically steady state has been reached.

This large ensemble of scenarios (298 simulations) spans a very wide range of climates. In the moist GCM simulations, the global-mean near-surface temperature varies from 253 to 312 K (287 K in the reference simulation), and the pole-to-equator temperature contrast

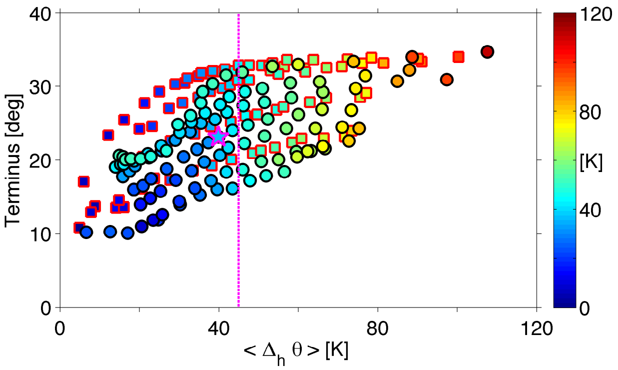

Figure 3.1: Latitude at the terminus of the Hadley circulation, versus the bulk meridional temperature contrast. Moist GCM simulations are indicated by the filled circles with black edges, and dry GCM simulations by filled squares with red edges. The moist GCM reference simulation ("Earth-like") is indicated by a pentagram with a magenta edge. The vertical magenta dashed-line indicates $\langle \Delta_h \theta \rangle = 45$ K. Colors refer to the bulk effective static stability contrast (units: [K]). This figure displays 80 dry GCM simulations and 109 moist GCM simulations, spanning a wide range of global-mean surface temperatures and pole-to-equator surface temperature contrasts (see section 3.3).

from 11 to 144 K (49 K in the reference simulation). In the dry GCM simulations, global-mean near-surface temperatures vary from 249 to 385 K, and pole-to-equator temperature contrasts from 12 to 90 K.

3.4 Results

3.4.1 The terminus of the Hadley circulation: description

Despite a large body of theoretical and observational studies, there is no unique definition for the terminus of the Hadley circulation (cf. Levine and Schneider, 2011). Here, we define the terminus as the subtropical latitude where the mean meridional mass flux, integrated from the 750 hPa pressure level to the the top of the atmosphere, attains 10% of its extremum value in the deep tropics. In most climates, the 750 hPa pressure level is near that where the mean meridional velocity reverses sign.

Figure 3.1 shows the latitude where the Hadley circulation terminates in both the dry and moist GCM simulations. The terminus shifts from 11° latitude for the narrowest cell to 35° latitude for the widest cell, spanning a range of nearly 25° in latitude. The most poleward latitude (i.e., 35° latitude) characterizes the Hadley circulation terminus in many simulations, which suggests the existence of a maximum extent. The maximum extent is quite apparent from Fig. 3.1 when noticing that the sensitivity of the terminus to climate changes is significantly smaller in scenarios with wide cells compared to those with narrow cells.

In the moist GCM simulations, the Hadley circulation widens when increasing either the longwave optical opacity or the insolation contrast (not directly apparent from Fig. 3.1): the widest cells generally correspond to climate scenarios with large longwave optical opacities and/or large insolation contrasts. In the dry GCM simulations, the Hadley circulation widens when either decreasing the convective lapse rate or increasing the pole-to-equator potential temperature contrast in radiative equilibrium (not directly apparent from Fig. 3.1). It is evident from Fig. 3.1 that dry and moist GCM simulations have comparable changes: even more so, the response of the terminus to increasing insolation contrast in the moist GCM is very similar to its response in the dry GCM to an increase in the pole-to-equator potential temperature contrast in radiative equilibrium; the same can be said of the response of the terminus to longwave optical opacity in the moist GCM compared to that of the convective lapse rate in the dry GCM.

The Hadley circulation in the reference climate (indicated by a pentagram in Fig. 3.1) is $24°$ wide in latitude; It is narrower than Earth's in the annual mean by about $6°$ latitude, which arises in part from a lack of ocean heat transport in these simulations: when either coupled to an idealized wind-driven ocean circulation or to an actual ocean GCM, the same moist GCM systematically produces climate scenarios with wider Hadley cells (e.g., compare Figs. 3.1 with Fig. 3.6), which are comparable to Earth's, when forced by Earth-like radiative parameters (cf. Levine and Schneider for a GCM study with an idealized wind-driven ocean transport; personal communication with Dr. T. M. Merlis for an ocean GCM study using the same moist GCM).

To study in details the climate sensitivity around the reference climate, the location of the terminus is shown on Fig. 3.3, for 2 sets of experiments: the first set corresponds to changing longwave optical opacity in scenarios with the reference insolation contrast ($\Delta_s = 1.2$); the second set corresponds to changing insolation contrast in scenarios with the reference longwave optical opacity ($\alpha = 1.0$). In the fist set, when increasing the longwave optical opacity, global-mean surface temperature increases by nearly 50 K while the pole-to-equator surface temperature contrast decreases by about 45 K; in the second set, when increasing the insolation contrast, global-mean surface temperature decreases by about 10 K while the pole-to-equator surface temperature contrast increases by nearly 75 K (cf. Fig. 3.3).

Consistent with Levine and Schneider (2011), the first set of experiment shows a widening of the Hadley circulation as the global-mean surface temperature increases and the pole-to-equator surface temperature contrast decreases. However, the second set of experiment shows a widening of the Hadley circulation despite the inverse temperature response

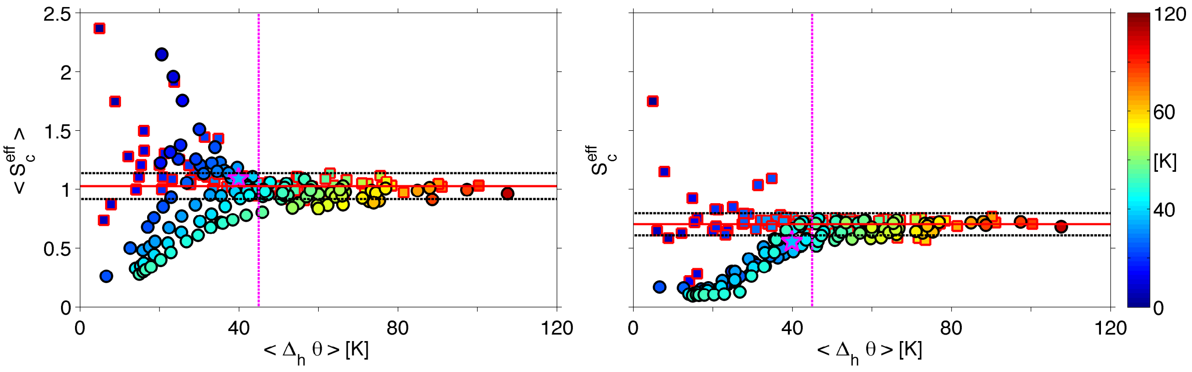

Figure 3.2: Bulk supercriticality (left panel), and supercriticality evaluated at the terminus of the Hadley circulation (right panel), versus the bulk meridional temperature contrast. The vertical magenta line ($\langle \Delta_h \theta \rangle = 45$ K) approximately delimitates two regions: in climate scenarios with bulk meridional temperature contrasts larger than this cutoff, $S_c^{\mathrm{eff}} \sim 1.0$ over the baroclinic zone and a constant value $S_c^{\mathrm{eff}} \leq 1.0$ characterizes the terminus of the Hadley circulation; in climate scenarios with bulk meridional temperature contrasts smaller than $\langle \Delta_h \theta \rangle = 45$ K, many simulations do not apparently satisfy these properties. The red solid line is the ensemble mean supercriticality, and the dashed black lines shows a width of 2 standard deviation from this ensemble mean, for all dry GCM simulations with bulk meridional temperature contrast larger than $\langle \Delta_h \theta \rangle = 45$ K. We estimate an ensemble mean of 1.02 for the left panel, and 0.70 for the right panel, consistent with these climate scenarios being controlled by baroclinic entropy fluxes; The standard deviation is 0.06 for the left panel and 0.05 for the right panel. Other plotting conventions follow from Fig. 3.1.

occurring, i.e., a (marginal) decrease in global-mean surface temperature and a (large) increase in the pole-to-equator surface temperature contrast. This seemingly contradictory behavior may be explained by investigating changes in the supercriticality at the terminus of the Hadley circulation.

3.4.2 Supercriticality: description

In a weakly nonlinear atmosphere controlled by baroclinic entropy fluxes, the terminus of the Hadley circulation corresponds to the most equatorward location where the thermal stratification adjusts to baroclinic waves. To test whether that is case, both in the dry and moist GCM simulations, effective supercriticality (S_c^{eff}) is evaluated locally at the terminus of the Hadley circulation and compared to its bulk estimate, as shown on Fig. 3.2.

At least two dynamical regimes are apparent from Fig. 3.2: In scenarios with large bulk meridional temperature contrasts ($\langle \Delta_h \theta \rangle \geq 45$ K), supercriticality values are clustered around an ensemble mean value, estimated at 1.02 for the bulk and 0.70 at the terminus of the Hadley circulation. In this regime, the data clustering distribution is quite narrow (the standard deviation is 0.06, about 10% variations around the mean), and does not seem to vary appreciably with climate changes. Thus, we find these climates to satisfy not only $\left\langle S_c^{\text{eff}} \right\rangle \sim 1$ in the baroclinic zone but also a constant value $S_c^{\text{eff}} \leq 1$ at the terminus of the Hadley circulation, which is consistent with the weakly-nonlinear flow regime described in Schneider and Walker (2006) and Korty and Schneider (2008). This flow regime characterizes scenarios with the widest Hadley cells (i.e., $35°$ wide in latitude), which indicates baroclinic wave adjustment as the key mechanism for setting a maximum extent for the Hadley circulation.

On the other hand, in scenarios with relatively small bulk meridional temperature contrasts ($\langle \Delta_h \theta \rangle \leq 45$ K), supercriticality is neither characterized by a constant ensemble mean value nor by a climate-invariant distribution broadness; this lack of invariance appears when evaluating both its bulk estimate and its value at the terminus. Yet, a qualitative difference between moist and dry GCM simulations is apparent in the behavior of supercriticality: while supercriticality generally decreases in the moist GCM simulations as the bulk meridional temperature contrast decreases, dry GCM simulations do not show any clear trend in this regime.

Supercriticality evaluated at the terminus of the Hadley circulation is shown on Fig. 3.3

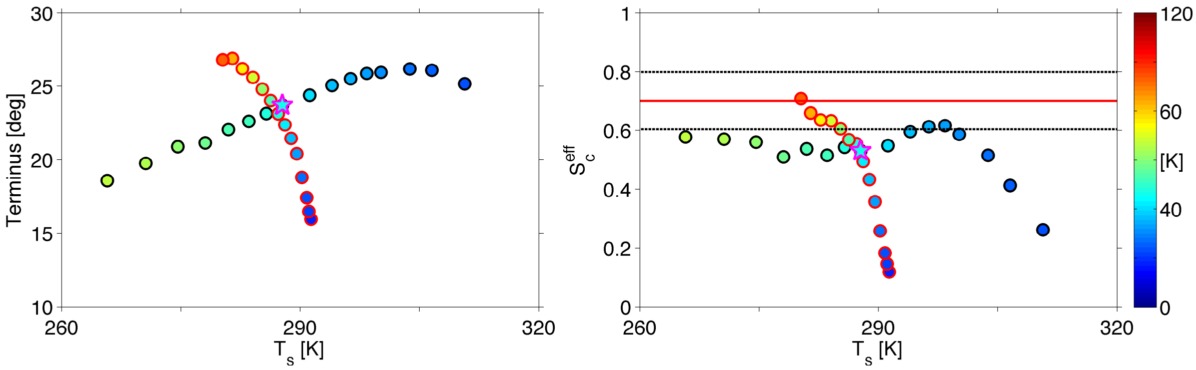

Figure 3.3: Latitude at the terminus of the Hadley circulation (left panel), and supercriticality at the terminus of the Hadley circulation (right panel), versus the global-mean surface temperature. Colors indicate the pole-to-equator temperature contrast. Other plotting conventions follow from Figs. 3.1 and 3.2.

for both climate change experiments around the reference simulation (described in section 3.4.1): as already apparent from Fig. 3.2, supercriticality in the reference simulation is nearly 2 standard deviations away from its ensemble mean values; this is perhaps not surprising considering that the bulk meridional temperature contrast is only 40 K, which is marginally below the empirical cutoff value $(45$ K$)$ for scenarios controlled by baroclinic waves. Fig. 3.3 shows that supercriticality converges toward the ensemble mean value 0.70 as insolation contrast increases, consistent with the bulk meridional temperature contrasts being larger ($\langle \Delta_h \theta \rangle \geq 45$ K). Low insolation contrasts are characterized by small supercriticality values, which corresponds to the climate scenarios found in the lower left corner of Fig. 3.2. In the global warming experiment, on the other hand, we find a relative invariance in supercriticality values, both at the terminus (Fig. 3.3) and as a bulk estimate (not shown), at least for simulations with global-mean surface temperature less than 300 K; in these scenarios, supercriticality at the terminus achieves an average value of 0.56, nearly identical to the 0.60 value used by O'Gorman (2010) to diagnose the terminus. Warm climates,

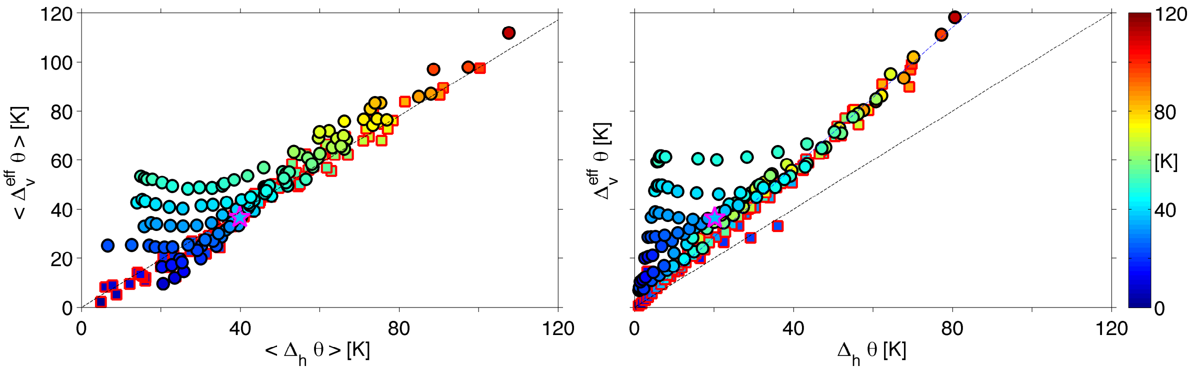

Figure 3.4: Bulk effective static stability contrast versus the bulk meridional temperature contrast (left panel), and effective static stability contrast versus the meridional temperature contrast, both evaluated at the terminus of the Hadley circulation (right panel). The black dashed line indicates a slope of 1.02 (both panels) and the blue dashed line indicates a slope of 0.70 (right panel only); scenarios in which the extratropical thermal stratification is controlled by baroclinic waves obey the linear relation described by the black line, when averaged over the baroclinic zone, and by the blue line, when evaluated at the terminus of the Hadley circulation. Strongly nonlinear scenarios, if any, would be found below the black (blue) line consistent with $S_c \gg 1$, while scenarios not controlled by baroclinic waves are found above the black (blue) line ($S_c \leq 1$). While nearly all dry GCM simulations may be considered to be in a weakly nonlinear flow regime dominated by baroclinic waves, moist GCM simulations share this property only for either relatively cold climates or climates with relatively large bulk meridional temperature contrasts; either warm or weakly differentially heated scenarios are not found to be controlled by baroclinic waves. Other plotting conventions follow from Fig. 3.1.

on the other hand, are characterized by smaller supercriticality values, as already shown in O'Gorman (2010). Thus, despite finding a value of supercriticality lower than that expected for scenarios dominated by baroclinic waves, we observe a relative invariance in the values of supercriticality at the terminus, in cold or temperate climate scenarios, similar to that found in simulations with large bulk meridional temperature contrasts ($\langle \Delta_h \theta \rangle \geq 45$ K).

3.4.3 Static stability and meridional temperature contrast

To investigate why supercriticality, either at the terminus of the Hadley circulation or as a bulk estimate, fails to diagnose a weakly nonlinear regime dominated by baroclinic waves in simulations with low bulk meridional temperature contrasts, the various factors composing supercriticality are plotted separately in Fig. 3.4. Consistent with the invariance of supercriticality in climates with large bulk meridional temperature contrasts ($\langle \Delta_h \theta \rangle \geq 45$ K), we find the effective static stability contrast to be linearly proportional to the meridional temperature contrast in many climate scenarios; The slope of this relation is 1.02 for the bulk estimates and 0.70 for the local estimates at the terminus.

Fig. 3.4 shows that dry GCM simulations follow this linear relation for the forcing parameters investigated in this study. This invariance is reconciled with the apparent data scattering shown on Fig. 3.4, at low bulk meridional temperature contrasts ($\langle \Delta_h \theta \rangle \leq 45$ K), by realizing that any computational uncertainty in diagnosing the bulk effective static stability contrast is amplified greatly when computing supercriticality for small values of the bulk effective static stability contrast; this is typically the case for the scattered data points shown on Fig. 3.4 as those correspond to scenarios with near-neutral extratropical lapse rates. Moist GCM simulations, on the other hand, show a clear departures from the the linear relation in scenarios with small bulk meridional temperature contrasts ($\langle \Delta_h \theta \rangle \leq 45$ K), consistently with the results shown on Fig. 3.4. There, the bulk effective static stability contrast is systematically larger than that predicted for weakly nonlinear scenarios dominated by baroclinic waves, and this bias increases with global-mean surface temperature; in particular, these large effective static stability contrasts are consistent with the small supercriticality values at the terminus found in the warmest simulations of the global warming experiment shown on Fig. 3.3.

3.5 Discussion

The thermal stratification appears to be controlled by baroclinic waves in the dry GCM simulations, even in scenarios with relatively weak thermal forcing. Yet, this is not necessarily the case in the moist GCM simulations: warm simulations, or simulations with weak differential heating, show large departure from the $\mathcal{O}(1)$ value achieved in scenarios controlled by baroclinic entropy fluxes. Clearly, water vapor dynamics is to blame for this departure, but it is unclear which of the assumption(s) used to derive supercriticality is violated in this regime: indeed, it may be that the diffusive behavior assumed in deriving supercriticality becomes invalid, or that the effective static stability fails to capture the interaction of precipitation with baroclinic waves, or that both of these properties fail. Further work is required to answer this question; yet it is plausible that updrafts shrink in size compared to downdrafts, implying larger values of the λ factor, similar to those found by O'Gorman (2010) in the tropical regions. This change in the relative size of the updrafts, in particular, would be qualitatively consistent with the regime transition observed by Lapeyre and Held (2004), using a 2-layer quasi-geostrophic model modified to crudely account for condensational heating: In this study, a regime transition was described, from a state where moist baroclinic waves have a dry-like geometry, with near-diffusive behavior, to a state characterized by a strong asymmetry between updrafts and downdrafts and lacking a diffusive behavior. While the former state is qualitatively consistent with the baroclinic wave dominated regime found in all our dry GCM simulations, the asymmetrical state might be relevant for describing the warm and weakly differentially heated moist GCM simulations characterized by $S_c^{\mathrm{eff}} \ll 1$.

The reference simulation, as well as many simulations in the global warming experiment shown on Fig. 3.3, appear to be at the junction between the weakly nonlinear regime dominated by baroclinic waves ($\left\langle S_c^{\mathrm{eff}} \right\rangle \sim 1$) described in Schneider and Walker (2006), and a more tropical-like regime perhaps similar to that described in Lapeyre and Held (2004). An identical reference simulation but with ocean heat transport in the low latitudes, which shows greater resemblance to Earth's in the annual mean, essentially provides the same result (shown in appendix 3.7.2). One practical implication of our findings is the need to study colder climates or climates with larger insolation contrasts when devising and testing various criteria for the termination of the Hadley circulation by baroclinic waves.

3.6 Conclusions

Using both a moist and a dry idealized GCM, we have simulated a large range of climates, changing dramatically both the global-mean surface temperature and the pole-to-equator surface temperature contrast. We find that the terminus of the Hadley circulation may vary over a large range of latitudes, both in dry and moist GCM simulations, shifting by nearly 25° in latitude. We have described an updated version of the supercriticality criterion, which accounts for a tight coupling of the thermal stratification in baroclinic updrafts to thermal convective plumes, and found it to be successful at diagnosing climate scenarios controlled by baroclinic waves. This criterion is also successful at diagnosing the Hadley circulation terminus, not only in nearly all climate scenarios obtained from a dry idealized GCM but also many scenarios obtained from a moist idealized GCM. This is consistent with previous theories that have described the Hadley circulation terminus as an equatorward boundary for baroclinic wave activity. On the other hand, in the moist GCM, the depth of the troposphere in relatively warm climates with small or modest meridional temperature contrasts appear to not be controlled by baroclinic waves. The Earth-like reference climate is at the junction between these 2 regimes. This calls for a better understanding of this regime, in which convective processes may be more active at organizing the large-scale dynamics. Further studies are required to improve our understanding of baroclinic eddies in a moist environment, and the interaction between stratiform and convective precipitation.

3.7 Appendix

3.7.1 Comparing static stabilities

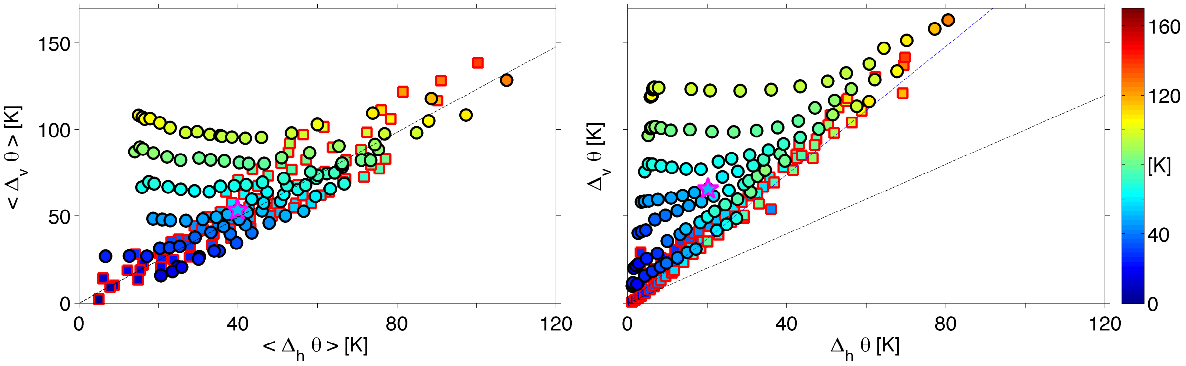

Figure 3.5: Bulk static stability contrast versus bulk meridional temperature contrast (left panel), and static stability contrast versus meridional temperature contrast, both evaluated at the terminus of the Hadley circulation (right panel). These panels differ from Fig. 3.2 and 3.4 by using the static stability contrast as defined by Schneider and O'Gorman (e.g., 2008) instead of the effective static stability contrast. Colors refer to the bulk static stability contrast (units: [K]). The black dashed line indicates the ensemble mean bulk supercriticality ($S_c = 0.81$), and the blue dashed line indicates the ensemble mean supercriticality at the terminus ($S_c = 0.54$), in dry GCM simulations with bulk meridional temperature contrast larger than 45 K. The standard deviation is 0.14 for the bulk estimate and 0.06 for the local estimate at the terminus. Other plotting conventions follow from Fig. 3.1 and 3.2.

Here, we compare the static stability contrast and the meridional temperature contrast, locally at the terminus of the Hadley circulation and in their bulk forms. Hence, the classical form of supercriticality, as described by Schneider and O'Gorman (2008), is compared to its effective form, as shown in Figs. 3.2 and 3.4. The classical form of supercriticality shows a relative climate invariance in scenarios with large bulk meridional temperature contrasts; at the terminus of the Hadley circulation, its behavior is nearly identical to its effective form, except for its ensemble mean, which is lower ($S_c = 0.54$ instead of $S_c^{\text{eff}} = 0.70$); classical bulk supercriticality, on the other hand, has a distribution spread that is nearly twice as large as that of its effective form; its ensemble mean is lower as well ($\langle S_c \rangle = 0.81$ instead of $\left\langle S_c^{\text{eff}} \right\rangle = 1.02$).

Thus, we find that introducing the effective static stability provides a clear advantage over using static stability itself, not only in the moist but also in the dry GCM simulations, when computing supercriticality.

3.7.2 Moist GCM simulations with ocean heat transport

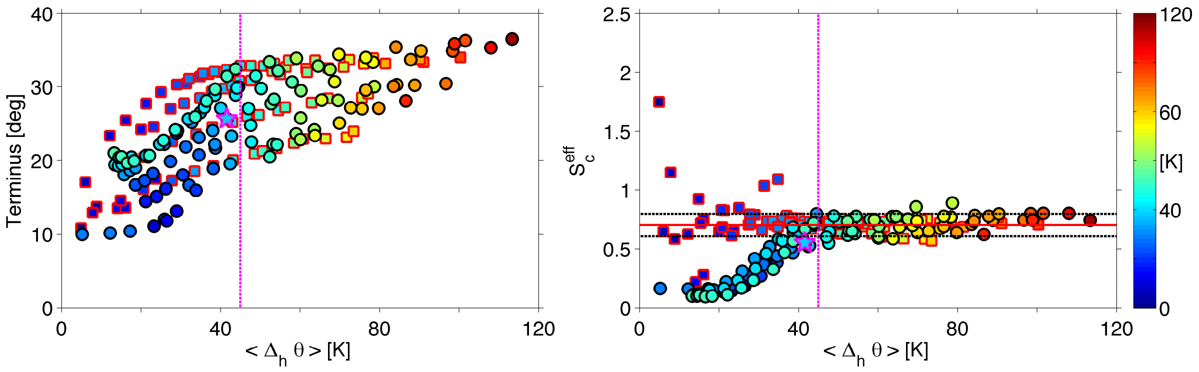

Figure 3.6: Latitude at the terminus of the Hadley circulation (left panel), and supercriticality at the terminus of the Hadley circulation (right panel), versus the bulk meridional temperature contrast, for simulations obtained from the moist GCM, as described in section 3.3.2, but incorporating a simple representation of ocean heat transport, as described in Levine and Schneider (2011). Other plotting conventions follow from Fig. 3.1 and 3.2.

Observational and modeling studies have shown that the wind-driven ocean heat transport forced by Ekman suction at the surface dominates the heat transport on Earth in the low-latitudes (Klinger and Marotzke, 2000; Held, 2001). Without such heat transport the flow regime in the upper troposphere is significantly different from that of Earth; in particular, not providing for ocean transport generally underestimates the effect of extratropical planetary waves on the extent and strength of the Hadley circulation (Herweijer et al., 2005). Hence, it is of primary interest for a modeler or a theorist to devise a representation for this component of the ocean circulation to account for its $\mathcal{O}(1)$ effects of the atmosphere and circumvent the painstaking computational needs of an ocean GCM. An analytical formulation can be devised for the energy carried by the zonal-mean component of the ocean circulation (Klinger and Marotzke, 2000; Held, 2001), which depends only the surface wind stress and the meridional sea surface temperature profile. Levine and Schneider (2011) added this simple ocean heat transport representation to the idealized moist GCM described in section 3.3.2 and found that many climatological features in the reference simulation, including the low-latitude momentum budget, bore greater resemblance to Earth's. Additionally, this ocean heat flux representation was shown to greatly affect the strength of the Hadley circulation, and to a lesser extent, its terminus as well. Thus, we have investigated whether large changes in the momentum balance in the tropics may affect the terminus of the Hadley circulation and its colocation with the onset of deep baroclinic waves. Figure 3.6 shows the latitude and supercriticality at the terminus of the Hadley circulation for a set of experiments identical to that shown on Fig. 3.1 apart from the ocean heat transport formulation described in Levine and Schneider (2011). Despite large difference in the strength of the Hadley circulations between slab and ocean simulations (slab and ocean refers to simulations without and with ocean heat transport respectively), we do not find similar discrepancies in the latitude of the terminus either at small or large bulk meridional temperature contrast. The terminus in each ocean simulation is generally a few degrees poleward of that of its corresponding slab simulation; yet, these changes are modest compared to strength of the Hadley circulation, which may be nearly halved when ocean heat transport is introduced. Figure 3.6 also shows that supercriticality in the ocean simulations behaves near identically in the slab and ocean simulations, with the overall distribution of supercritical values and its ensemble mean being identical at the terminus of the Hadley circulation.

Thus, we find that large changes in the deep tropics, such as changes in the strength of Hadley circulation, are not correlated with similar changes in the terminus of the Hadley circulation. However, the terminus is still characterized by a relatively invariant value of supercriticality; this essentially confirms that the location of the terminus is directly controlled by baroclinic waves, and not directly by changes in deep tropical heating, which exerts a large control on the strength of the Hadley circulation.

Chapter 4

A Single-Layer Model of the Tropical Atmosphere: the Hadley Circulation over a Wide Range of Climate Changes

4.1 Introduction

A large set of idealized GCM have shown that the strength and extent of the Hadley circulation can vary dramatically when varying insolation and longwave optical opacity (Levine and Schneider, 2011). These changes are qualitatively consistent with those found in more comprehensive GCM simulations for climate changes around an Earth-like simulation (e.g., Lu et al., 2007). Yet, these changes remain poorly understood; in particular, it is unclear how eddy activity in the extratropics influences the dynamics of the Hadley circulation, and thus what it implies for changes in the strength and extent of these cells with climate changes. Both the mean meridional flow in the tropics and the eddy activity in the extratropics may experience large changes with global climate change (Levine and Schneider, 2011); yet, it is unclear whether or how these changes in eddy activity may feedback on the low-latitude dynamics. It is not possible, however, to disentangle these effects from GCM simulations alone.

In this study, we design an axisymmetric model that is coupled to simple representations for eddy fluxes, in an attempt to take advantage of the simplicity provided by an axisymmetric model, while also accounting for the influence exerted by eddies on the momentum and thermodynamic tropospheric budgets. Results from this model are compared to a wide range of climates obtained from an idealized GCM, when forced by varying the insolation and longwave optical opacity of the atmosphere.

4.2 Single-layer model (SLM): Description

The single-layer model (SLM) solves for an axisymmetric circulation, in which the meridional flow is confined to layers of uniform thickness and height located just below the tropopause and just above the surface. Indeed, the SLM takes advantage of the fact that mass and energy fluxes are generally confined to relatively thin layers located just above the surface and just below the tropopause (see Fig. 4.1). The thickness of the upper layer is set to a constant for all climates. The dynamics is forced by relaxing temperature toward a radiative-convective equilibrium profile, which corresponds to a prescribed radiative forcing. Eddy fluxes are parameterized as a function of mean flow quantities and depend on an eddy velocity, which may vary with climates. In this study, this eddy velocity is taken from corresponding eddy-resolving GCM simulations, which allows for an evaluation of the relative importance of extratropical wave activity in setting the strength and extent of the Hadley circulation.

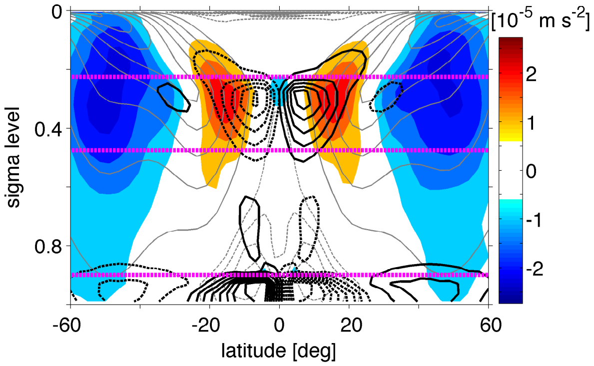

Figure 4.1: Cartoon of SLM dynamics overlaying the time and zonal-mean dynamics in an Earth-like reference climate, obtained from the idealized GCM described in appendix 4.7.2. Colors indicate the horizontal component for eddy momentum flux divergence ($\partial_y \overline{u'v'} \geq 0$, red colors) and convergence ($\partial_y \overline{u'v'} \leq 0$, blue colors). Overbars define a time and zonal mean over a period of 4 years in steady state, and primes are deviations from the mean. Thin gray lines show the mean zonal wind ($\overline{u}$), and black lines the mean meridional wind ($\overline{v}$); solid and dashed lines indicate positive and negative values respectively for both wind components. Values for the zonal wind are spaced by intervals of $10\,\mathrm{m\,s^{-1}}$, while those of the meridional wind are spaced by interval of $0.7\,\mathrm{m\,s^{-1}}$. The magenta lines demarcate the regions over which dynamics is solved in our simple model of the atmosphere described in section 4.2. The top magenta line is a global-mean tropopause height, which we estimate from a simple radiative-convective calculation; the magenta line just below indicates the lower boundary of the upper layer, which encompasses 25% of the atmosphere in mass. This upper layer contains most of the meridional mass flux of the free troposphere, consistent with planetary waves there fluxing large amount of momentum from the subtropics to the midlatitudes. This free tropospheric mass flux is compensated by a return flow in the boundary layer, which is confined between the surface and the lowest magenta line.

4.2.1 Coordinates

The SLM is a two-dimensional model, and thus requires defining a meridional and vertical coordinate. The meridional coordinate y is a linear approximation for the spatial distance between the equator and a point located at a latitude φ,

$$y = a\varphi. \tag{4.1}$$

Here, a the radius of the planet. The vertical coordinate Z is the log-p height defined as

$$Z = -Z_o \log \frac{p}{p_o}, \tag{4.2}$$

and depends on the mean surface pressure p_o and a prescribed scale-height Z_o,

$$Z_o = \frac{r_d T_o}{g}, \tag{4.3}$$

where T_o is a reference temperature, r_d the gas constant for dry air, and g the gravitational acceleration.

4.2.2 Zonal momentum budget

The time and zonal-mean zonal momentum budget in the upper layer may be expressed as follows:

$$\partial_t \left[\overline{u}\right] + \left[\overline{v}\partial_y \overline{u}\right] + \left[\overline{w}\partial_Z \overline{u}\right] - f\left[\overline{v}\right] = -\partial_y \left[\overline{u'v'}\right] - \partial_Z \left[\overline{u'w'}\right]. \tag{4.4}$$

Here, u is the zonal velocity, and v and w are the meridional and vertical velocities respectively. f is the Coriolis parameter, defined as

$$f = 2\Omega \frac{y}{a}, \tag{4.5}$$

where Ω is the rotation rate of the planet. A time and zonal average is defined as $\overline{(.)}$, and $[(.)]$ defines a mass-weighted vertical average over the upper layer,

$$[(.)] = \frac{1}{\Delta p_t} \int_{p_T}^{p_B} (.) \; \mathrm{d}p, \tag{4.6}$$

with p_T and p_B defining the pressure at the top and bottom of the upper layer, whose mass thickness

$$\Delta p_t = p_B - p_T \tag{4.7}$$

is set to a constant value (see Table 4.1).

On the left-hand side (LHS) of Eqn. 4.4, mean flow contributions to the zonal momentum budget are represented by the mean meridional advection of mean zonal momentum (second term), the mean vertical advection of mean zonal momentum (third term), and the mean meridional advection of planetary angular momentum (fourth term). On the right-hand side (RHS) of Eqn. 4.4, eddy contributions to the zonal momentum budget are separated into a component associated with meridional (first term) and vertical fluxes (second term).

Mean flow contributions to the zonal momentum budget can be discretized, ignoring vertical variations in the zonal and meridional wind in the upper layer, as follows:

$$\partial_t u_t + v_t \partial_y u_t + \ldots - f v_t = \ldots \tag{4.8}$$

Here, u_t and v_t are the zonal and meridional wind averaged over the upper layer, respectively.

To discretize the mean vertical advection of mean momentum, we limit momentum transfer to updrafts consistently with vertical velocities vanishing at the top of the upper layer,

$$[\overline{w}\partial_Z\overline{u}] = \mathcal{H}(w_B)\, w_B\, \partial_Z u\mid_B, \tag{4.9}$$

where $(.)\mid_B$ indicates that quantities are evaluated at level Z_B, corresponding to the pressure level p_B defining the bottom of the upper layer. The Heaviside function $\mathcal{H}$ selectively removes downdrafts from the momentum budget. The vertical velocity at the bottom of the upper layer (Z_B) in regions of updrafts may be obtained from the necessary balance existing between meridional mass flux divergence (convergence) in the upper layer and updrafts (downdrafts) at the base of the upper layer,

$$w_B = (Z_T - Z_B)\,\partial_y v_t. \tag{4.10}$$

Considering the vertical zonal wind shear to be invariant in height, and assuming negligible surface winds

$$\partial_z u\mid_B = \frac{u_t}{Z_T}, \tag{4.11}$$

the mean vertical mean zonal momentum advection is recast as follows:

$$[\overline{w}\partial_z\overline{u}] = \frac{(Z_T - Z_B)}{Z_T}\, u_t\, \partial_y v_t\, \mathcal{H}(\partial_y v_t). \tag{4.12}$$

To represent the meridional transfer of momentum from the eddies to the mean flow, we use the empirical formulation devised by Sobel and Schneider (2009), which is parameterized as follows:

$$\partial_y \left[\overline{u'v'}\right] = v_u \, \partial_y u_t \, \mathcal{S}(y). \tag{4.13}$$

Here, v_u is an eddy velocity, which is set to a constant value for each climate. The sign function $\mathcal{S}$ is defined as

$$\mathcal{S}(y) = \mathrm{sgn}(y). \tag{4.14}$$

The vertical transfer of momentum is parameterized as a Rayleigh drag,

$$\partial_z \left[\overline{u'w'}\right] = \epsilon u_t, \tag{4.15}$$

where ϵ is the damping coefficient. This simple representation relaxes the zonal wind in the upper layer toward 0, consistent with zonal wind being significantly smaller near the surface compared to that in the upper troposphere.

4.2.3 Meridional momentum budget

The time and zonal-mean meridional momentum budget averaged over the same upper layer may be expressed as follows:

$$\partial_t \left[\overline{v}\right] + \left[\overline{v}\partial_y\overline{v}\right] + \left[\overline{w}\partial_Z\overline{v}\right] + f\left[\overline{u}\right] + \left[\partial_y\overline{\phi}\right] = -\partial_y \left[\overline{v'v'}\right] - \partial_Z \left[\overline{v'w'}\right]. \tag{4.16}$$

Here, ϕ is the geopotential height. On the left-hand side of Eqn. 4.16, the mean flow contributions to the mean meridional momentum budget are represented by the advection of meridional momentum by the mean meridional flow (second term), the mean vertical advection of mean meridional momentum (third term), the Coriolis acceleration related to the mean zonal wind (fourth term), and the meridional acceleration associated with an existing thermal gradient (fifth term). On the right-hand side, eddy contributions are shown decomposed into meridional and vertical components (first and second term respectively).

All vertical advection terms are neglected. Consistent with the discretization used to cast the mean advection terms in the zonal momentum budget, mean flow quantities are expressed as follows:

$$\partial_t v_t + v_t \partial_y v_t + f u_t + \ldots = \ldots \tag{4.17}$$

The geopotential gradient in Eqn. 4.16 may be recast in terms of temperature using hydrostatic balance,

$$\partial_Z \overline{\phi} = -\frac{r_d \overline{T}}{Z_o}, \tag{4.18}$$

where T is the temperature. Thus, integrating the hydrostatic balance from a low-tropospheric level to the top of the layer, we obtain

$$\overline{\phi}_T - \overline{\phi}_S = -r_d \frac{\{\overline{T}\}}{Z_o} \left(Z_T - Z_S\right), \tag{4.19}$$

where ϕ_T and ϕ_S refers to the geopotential height at top of the layer (Z_T) and just above the surface (Z_S) respectively. Here, $\{(.)\}$ defines a vertical log-pressure weighted average from a near-surface level (Z_S) to the top of the thin layer (Z_T):

$$\{(.)\} = \frac{1}{Z_T - Z_S} \int_{Z_S}^{Z_T} (.)\, \mathrm{d}Z, \tag{4.20}$$

Neglecting latitudinal variations in the near-surface geopotential height (consistent with neglecting near-surface winds), the thermal gradient

$$\left[\partial_y \overline{\phi}\right] \simeq \partial_y \overline{\phi}_T \simeq r_d\, \partial_y \left\{\overline{T}\right\} \frac{Z_T}{Z_o} \tag{4.21}$$

is expressed in terms of the averaged tropospheric temperature.

The meridional component of meridional momentum transfer is represented as a diffusive process, i.e.,

$$\partial_y \left[\overline{v'v'}\right] = -\kappa_v \partial_y^2 v_t, \tag{4.22}$$

where κ_v defines the eddy diffusivity coefficient for this process.

4.2.4 Thermodynamic budget

The time and zonal-mean column-averaged enthalpy budget can be expressed as follows:

$$\partial_t \langle s \rangle + \partial_y \left\langle \overline{v}\, \overline{h} \right\rangle = Q_h + Q_o - \partial_y \left\langle \overline{v'h'} \right\rangle . \tag{4.23}$$

Here, s is the moist enthalpy:

$$s = c_p T + L_v q, \tag{4.24}$$

where q is the specific humidity, c_p the specific heat capacity for dry air at constant pressure, and L_v the latent heat of vaporization; h is the moist static energy:

$$h = c_p T + \phi + L_v q. \tag{4.25}$$

And $\langle(.)\rangle$ defines a mass-weighted vertical average, from the surface to the top of the atmosphere,

$$\langle(.)\rangle = \frac{1}{p_o} \int_0^{p_o} (.) \; \mathrm{d}p. \tag{4.26}$$

The enthalpy budget may be modified by the mean meridional circulation (second term on RHS of Eqn. 4.23), by eddy transport (third term on RHS) as well as by vertical fluxes at surface (second term on LHS) and at the top of the atmosphere (first term on LHS).

The mean advection of moist static energy is represented by an overturning cell acting on a preexisting thermal contrast between the upper and lower troposphere:

$$\partial_y \left\langle \overline{v}\, \overline{h} \right\rangle = \partial_y \left(\delta_t \, v_t \Delta h \right). \tag{4.27}$$

Here, δ_t is the normalized mass thickness of the thin layer, defined as

$$\delta_t = \frac{\Delta p_t}{p_o}, \tag{4.28}$$

and Δh defines a contrast in moist static energy between the upper layer and lower layer of the troposphere. We define this vertical thermal contrast as the gross moist stability of the atmosphere (GMS).

Enthalpy fluxes at the surface (Q_o) correspond to the energy flux diverged by an ocean circulation; in this study it is set to 0. Enthalpy fluxes at the top of the atmosphere correspond to a radiative imbalance between incoming insolation and outgoing shortwave radiation,

$$Q_h = (SW^{TOA} - LW^{TOA})\frac{g}{p_o}. \tag{4.29}$$

Here, SW^{TOA} is the incoming insolation, and LW^{TOA} is the outgoing longwave radiation. While incoming insolation (SW^{TOA}) is an external forcing, outgoing longwave radiation (LW^{TOA}) depends on the temperature and longwave optical opacity of the atmosphere. The adjustment of outgoing longwave radiation may be represented by a linear perturbation from a reference state:

$$Q_h = \alpha_r \left(\langle T \rangle - \langle T \rangle_E\right). \tag{4.30}$$

Here, α_r defines the outgoing longwave radiation sensitivity to changes in the column-averaged temperature, and $\langle T \rangle_E$ is the column-averaged temperature profile in radiative-convective equilibrium.

Representing the eddy moist static energy flux divergence (third term on RHS) requires considering separately the energy transport associated with dry air and moisture, i.e.,

$$\partial_y \left\langle \overline{v'h'} \right\rangle = \partial_y \left\langle \overline{v'h'_d} \right\rangle + \partial_y \left\langle \overline{v'h'_m} \right\rangle . \tag{4.31}$$

Here, h_d is the dry component of moist static energy,

$$h_d = c_p T + gz, \tag{4.32}$$

and h_m its moisture component,

$$h_m = L_v q. \tag{4.33}$$

One one hand, the eddy dry static energy flux is parameterized as a diffusive process, which diffuses dry enthalpy:

$$\partial_y \left\langle \overline{v'h'_d} \right\rangle = -\kappa_h c_p \partial_y^2 \left\langle T \right\rangle \delta_h. \tag{4.34}$$

Here, κ_h is the eddy diffusivity coefficient associated with this process and δ_h is the normalized mass thickness of the layer over which diffusion occurs.

The moisture component, on the other hand, is parameterized by considering separately precipitation and evaporation, i.e.,

$$\partial_y \left\langle \overline{v\, h_m} \right\rangle = L_v (E - P) \frac{g}{p_o}, \tag{4.35}$$

where P is the local precipitation rate and E the local evaporation rate. Evaporation is assumed to be constant in latitude, i.e.,

$$E = \left\| E \right\| . \tag{4.36}$$

Here, $\left\| (.) \right\|$ defines a global average. Precipitation itself can be decomposed into convective and stratiform precipitation:

$$P = P_{cv} + P_{cd}. \tag{4.37}$$

Here, P_{cv} refers to convective precipitation, P_{cd} to stratiform precipitation. We assume that convective precipitation is primarily associated with the mean meridional advection of moisture: this is borne out by observing that the maximum in convective precipitation in the deep tropics and its minimum in the subtropics are colocated with regions of convergence and divergence of moisture by the mean meridional flow. There, downwelling in the subtropics inhibits convection, and upwelling in the deep tropics promotes convection, creating a precipitation maximum in the deep tropics and a minimum in the subtropics. The mean meridional advection of moisture thus may be expressed as

$$\partial_y \left\langle \overline{v}\,\overline{h_m} \right\rangle = L_v \left(\alpha \left\| E \right\| - P_{cv} \right) \frac{g}{p_o}, \tag{4.38}$$

where α is a factor quantifying the ratio of convective to total precipitation globally:

$$\alpha = \frac{\left\| P_{cv} \right\|}{\left\| E \right\|}. \tag{4.39}$$

This factor α assumes a value between 0 and 1. In an Earth-like climate, this factor is near 75%, indicating that convective precipitation accounts for nearly three-quarters of all precipitation globally.

Stratiform precipitation, on the other hand, is associated primarily with eddy moisture fluxes: in the midlatitudes, in particular, stratiform precipitation peaks in the storm track region, which also corresponds to a maximum convergence of moisture by baroclinic eddies. This coupling between eddy moisture flux and stratiform precipitation is expressed as follows:

$$\partial_y \left\langle \overline{v'h'_m} \right\rangle = L_v \left((1-\alpha) \|E\| - P_{cd} \right) \frac{g}{p_o}. \tag{4.40}$$

To estimate the local and global amount of water rained in stratiform clouds, one needs to consider the physical processes tying stratiform precipitation to geostrophic eddies.

Baroclinic eddies advect water vapor from the subtropical lower troposphere, which is displaced near adiabatically poleward until reaching saturation; there precipitation occurs on the scale of the cyclonic core. O'Gorman and Schneider (2008b) found a representation for the mean condensation rate associated with baroclinic waves,

$$c = \left| \partial_y q^* \ |_\theta \right| \sqrt{\overline{v'^2}} \exp\left(-\frac{d^2}{2L_e^2} \right). \tag{4.41}$$

Here, c is the local mean condensation rate in stratiform clouds, $\partial_y q^* \ |_\theta$ is the meridional gradient of saturation specific humidity along an isentropic surface, $\sqrt{\overline{v'^2}}$ is the root mean square (RMS) eddy meridional velocity, L_e is the rms meridional displacement of air parcels before irreversible effects become dominant, and d is the distance an air parcel has to be displaced to just become saturated locally. The exponential factor depends primarily on the relative humidity along the path of an air parcel, which may vary with latitude: in a saturated atmosphere, this factor equals 1, while it vanishes in a dry atmosphere. We assume stratiform clouds to be confined to a layer of constant normalized mass thickness δ_{cd}. To simplify Eqn. 4.41 further, variations in the exponential factor, both in latitude and with climate changes, are neglected, as well as latitudinal variations in the RMS eddy velocity. We assume the saturated specific humidity gradient in the condensational layer to be proportional to that of the column-averaged specific humidity. These assumptions are summarized as follows:

$$P_{cd} = \frac{p_o}{g}\, F_m\, v_h\, \partial_y \left\langle q \right\rangle \mathcal{S}(y), \tag{4.42}$$

where

$$F_m = \varrho \delta_{cd} \exp\left(-\frac{d^2}{2L_e^2}\right). \tag{4.43}$$

Here, ϱ is the constant of proportionality between the specific humidity in the condensational layer and its column-averaged value; v_h is an eddy velocity corresponding the eddy rms velocity shown in Eqn. 4.42. Eqn. 4.42 can be simplified further by assuming a linear dependence between the column-averaged specific humidity and the column-averaged temperature as follows:

$$\left\langle q \right\rangle = \left\langle q \right\rangle_r + \gamma_r \left(\left\langle T \right\rangle - \left\langle T \right\rangle_r \right). \tag{4.44}$$

Here, γ_r defines the sensitivity of column-averaged specific humidity ($\langle q \rangle$) to changes in column-averaged temperature ($\langle T \rangle$), around a reference state with given values of temperature ($\langle T\rangle_r$) and specific humidity ($\langle q\rangle_r$). This moisture factor varies strongly with temperature according to the Clausis-Clayperon relation,

$$\gamma_r = \frac{d\,\langle q\rangle}{d\,\langle T\rangle} \approx \frac{L_v\,\langle q\rangle}{r_v\,\langle T\rangle^2}, \tag{4.45}$$

with r_v defining the gas constant for water vapor. Using the linear dependence of specific humidity on temperature, large-scale precipitation may be expressed as

$$P_{cd} = \frac{c_p}{L_v}\,\frac{p_o}{g}\,\delta_m\,v_h\,\partial_y\,\langle T\rangle\,\mathcal{S}(y), \tag{4.46}$$

where δ_m is defined as

$$\delta_m = \frac{L_v}{c_p}\,\gamma_r\,F_m. \tag{4.47}$$

Hence, a global-mean value for stratiform precipitation is obtained as follows:

$$\|P_{cd}\| = (1-\alpha)\,\|E\| = \frac{c_p}{L_v}\,F_m\,v_h\,\frac{\Delta\,\langle T\rangle}{a}. \tag{4.48}$$

Here, ΔT is the equator-to-pole temperature contrast. Combining its dry and moisture components, the total eddy moist static energy flux divergence may be expressed as

$$\partial_y\left\langle\overline{v'h'}\right\rangle \;=\; c_p\delta_h\left(\kappa_h\partial_y^2\,\langle T\rangle - \frac{\delta_m}{\delta_h}\,v_h\left(\partial_y\,\langle T\rangle\,\mathcal{S}(y) - \frac{\Delta\,\langle T\rangle}{a}\right)\right). \tag{4.49}$$

To relate the zonal and meridional momentum budgets in the upper layer (Eqns. 4.4

and 4.16 respectively) to that of the vertically averaged enthalpy budget (Eqn. 4.23), the mass-weighted and log mass-weighted temperature are set to be equal, i.e.,

$$\{T\} = \langle T\rangle \, . \tag{4.50}$$

Eddy velocities and diffusivity coefficients are assumed to be proportional to one another, i.e.,

$$\kappa_h = \kappa_e = \mathcal{L}_\mathrm{e}\, v_e \quad \text{and} \quad \kappa_v = \kappa_e, \tag{4.51}$$

where $\mathcal{L}_\mathrm{e}$ is and eddy lengthscale, and

$$v_h = v_e \quad \text{and} \quad v_u = \varsigma v_e, \tag{4.52}$$

where ς is a climate-invariant coefficient.

4.2.5 Summary

We can thus summarize the 3 budgets used in the SLM:

$$
\begin{cases}
\partial_t u_t + v_t \partial_y u_t + \frac{(Z_T - Z_B)}{Z_T} u_t \partial_y v_t \mathcal{H}(\partial_y v_t) - f v_t = -v_u \, \partial_y u_t \mathcal{S}(y) - \epsilon u_t, \\
\\
\partial_t v_t + v_t \partial_y v_t + f u_t + r_d \partial_y \left\langle T \right\rangle \frac{Z_T}{Z_o} = \kappa_v \partial_y^2 v_t, \\
\\
c_p \partial_t \left\langle T \right\rangle + \partial_y \left(\delta_t v_t \Delta h \right) = Q_h + Q_o + Q_e,
\end{cases}
\tag{4.53}
$$

with

$$
\begin{cases}
Q_h = \alpha_r \left(\left\langle T \right\rangle - \left\langle T \right\rangle_E \right), \\
\\
Q_e = c_p \delta_h \left(\kappa_h \partial_y^2 \left\langle T \right\rangle - \frac{\delta_m}{\delta_h} v_h \left(\partial_y \left\langle T \right\rangle \mathcal{S}(y) - \frac{\Delta \left\langle T \right\rangle}{a} \right) \right).
\end{cases}
\tag{4.54}
$$

4.3 Experiments description

In this study, we investigate the response of the dynamics in the SLM to changes in both the longwave optical opacity and insolation contrast. To simulate these climate changes, a handful of external parameters are varied to account for changes in the radiative and thermodynamic properties of the atmosphere. This set of thermal parameters is complemented in each climate by an eddy velocity, which corresponds to the eddy activity associated with this set of thermal parameters. The eddy velocity is estimated using a GCM, which resolves eddy fluxes for any given set of thermal parameters prescribed in the SLM. We describe,

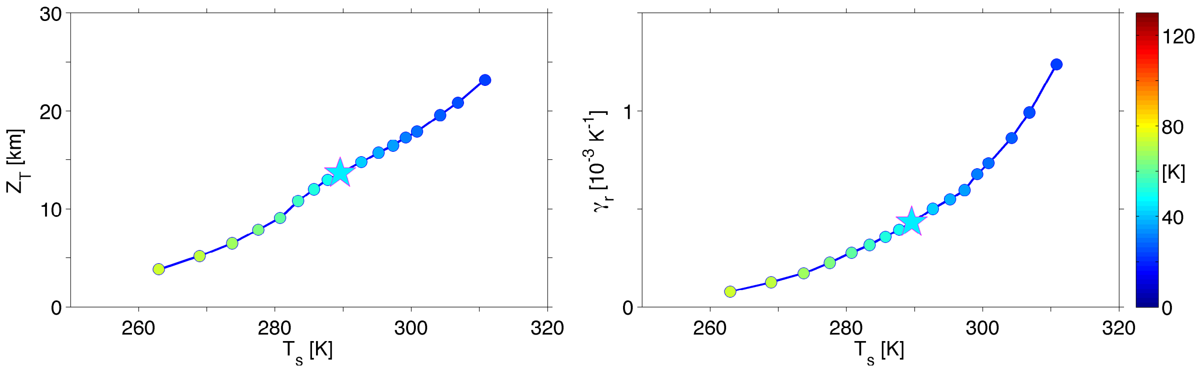

Figure 4.2: Tropopause height and moisture sensitivity to temperature changes, in a set of radiative-convective simulation, forced by a global-mean value of insolation, as a function of the global-mean surface temperature. Colors show the pole-to-equator temperature contrast in the moist GCM simulations corresponding to these values of tropopause height and moisture sensitivity factor. A pentagram indicates the value of the tropopause height and moisture sensitivity factor corresponding to Earth-like values of insolation contrast and longwave optical opacity.

in more detail, how both thermal and eddy parameters are estimated over a wide range of climates.

4.3.1 Thermal parameters (direct forcing)

Changes in the longwave optical opacity and insolation can be represented in the SLM by varying the vertically integrated radiative equilibrium temperature profile ($\langle T \rangle_E$), the height of the upper-layer (Z_T) as well as the moisture sensitivity to changes in temperature (γ_r). We estimate these thermal parameters, and their sensitivities to changes in either insolation contrast or longwave optical opacity, by considering their profiles in radiative-convective equilibrium. It implies, alternatively, that these thermal parameters are considered to be independent of the large-scale dynamics.

At least 2 arguments can be made in support of neglecting the effects of the large-scale dynamics on these thermal parameters. First, the vertically averaged temperature profile is relatively close to its profile in radiative-convective equilibrium, to which it must relax in the limit of a vanishing large-scale dynamics. Comparing temperature profiles in radiative-convective equilibrium to the corresponding ones in dynamical equilibrium, we find this assumption to generally hold well, especially in scenarios with small and modest pole-to-equator temperature contrasts. Second, the lapse rate in the tropics is close to that in the deep tropics, due to temperature contrasts being weak across the tropics (Sobel et al., 2001). It implies that, at least across the tropical regions, the climate sensitivity of these thermal parameters ought to be set by their climate sensitivities in the deep tropics. There, the lapse rate is essentially in convective equilibrium with the local surface temperature (e.g., Arakawa and Schubert, 1974), which is virtually equal to a radiative-convective equilibrium lapse rate, due to the short adjustment timescale of convection compared to either radiative or dynamical processes on the large scale.

Using a GCM modified to run in radiative-convective equilibrium (see appendix 4.7.2), we estimate the radiative-convective equilibrium temperature profile, which varies with prescribed insolation and longwave optical depth profiles. Using the same model, we evaluate the tropopause height, as well as the sensitivity of moisture and outgoing longwave radiation to temperature changes, at the latitude where insolation equals its global mean value. At this location, values for surface temperature and (radiative-convective) lapse rate are comparable to those in the deep tropics in dynamical equilibrium. Here, it is assumed that the height of the upper level, as well as the sensitivity factors for moisture content and outgoing longwave radiation, remains independent of insolation contrast, as long as it does not change its global-mean value. Surface temperature in the deep tropics is indeed found to be more sensitive to its global mean than its pole-to-equator contrast value.

Figure 4.2 shows the behavior of the tropopause height and sensitivity coefficient for moisture for all longwave optical opacity profiles, as estimated from the radiative-convective equilibrium state described above. Not shown is the sensitivity coefficient for outgoing longwave radiation, which was found to be nearly invariant over this range of climate changes (see value in Table 4.1). Both the tropopause height and moisture sensitivity coefficients are found to increase as climate warms: yet, the tropopause height increases nearly linearly with global-mean surface temperature, while the sensitivity coefficient for moisture has a near exponential increase consistent with the Clausius-Clayperon scaling (e.g., Schneider et al., 2010). At the reference climate, we find a value of $15\,\mathrm{km}$ for the tropopause height and a moisture sensitivity of about $6\%\,\mathrm{K}^{-1}$, consistent with their values in Earth's present climate.

4.3.2 Eddy parameter (eddy-mediated forcing)

Changes in thermal parameters, driven by changes in optical depth and insolation contrast, are complemented by varying the eddy velocity, which characterize the transport of momentum and moist static energy in the SLM. We estimate this eddy velocity by evaluating the degree of eddy activity in an eddy-resolving model and converting this quantity into an effective mixing velocity. For every set of thermal parameters shown in section 4.3.1, the barotropic component of the eddy kinetic energy is evaluated globally in the corresponding (eddy-resolving) GCM simulation. This global-mean kinetic energy is then converted into an effective eddy mixing velocity,

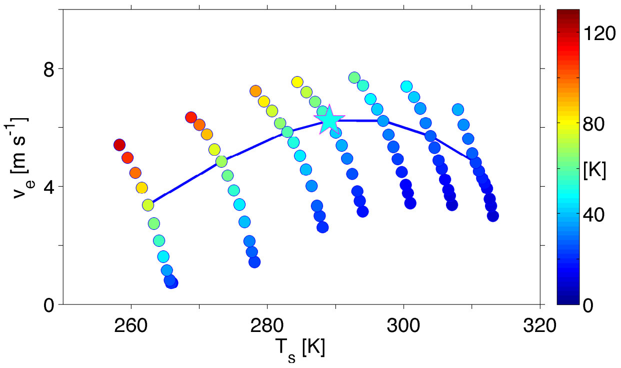

Figure 4.3: Eddy velocity, as estimated in Eqn. 4.55, as a function of the global-mean surface temperature in the moist GCM simulations. Colors show the pole-to-equator temperature contrast in the moist GCM simulations. A pentagram indicates the Earth-like reference simulation, plotted in Fig. 4.4. The solid blue line shows the global warming experiment obtained by increasing longwave optical opacity and keeping insolation to its Earth-like profile.

$$v_e = \|\mathrm{EKE}_{\mathrm{baro}}\|^{1/2}. \tag{4.55}$$

Here, $\|(.)\|$ defines a global average; $\mathrm{EKE}_{\mathrm{baro}}$ is the barotropic component of the eddy kinetic energy. A globally integrated value of the eddy kinetic energy was found to be adequate for estimating eddy transport on global scales (e.g., water vapor transport in O'Gorman and Schneider, 2008b). The barotropic component of the eddy kinetic energy is associated with geostrophic motion, which occurs primarily on the scale of the Rossby deformation radius, and thus better captures turbulent mixing on planetary scales (Schneider and Walker, 2006).

Figure 4.3 shows the variations of the eddy velocity, as computed in Eqn. 4.3, for all climate scenarios. On one hand, eddy velocity is found to increase steadily as the insolation profile steepens; on the other hand, it follows a nonmonotonic behavior as the global-mean surface temperature increases, consistent with the behavior observed in O'Gorman and

Parameter	Value	Unit	Definition
c_p	1004	$\mathrm{J\,kg^{-1}\,K^{-1}}$	Specific heat capacity for dry air at constant pressure
r_d	287	$\mathrm{J\,kg^{-1}\,K^{-1}}$	Gas constant for dry air
L_v	2.5×10^6	$\mathrm{J\,kg^{-1}}$	Latent heat of vaporization
g	9.8	$\mathrm{m\,s^{-2}}$	Gravitational acceleration
a	6.37×10^6	m	Radius of planet
Ω	7.23×10^{-4}	$\mathrm{s^{-1}}$	Rotation rate of planet
T_o	300	K	Reference temperature
α_r	4.0	$\mathrm{W\,m^{-2}\,K^{-1}}$	OLR sensitivity to changes in $\langle T \rangle$
$\mathcal{L}_e$	6.0×10^6	m	Eddy lengthscale over which dry enthalpy is diffused
ϵ_u	10^{-10}	$\mathrm{s^{-1}}$	Rayleigh drag for zonal wind
ε_u	0.10	–	Rescaling coefficient for eddy velocity in zonal momentum budget
δ_t	0.25	–	Normalized mass thickness of upper layer
δ_d	0.05	–	Normalized mass thickness of diffusive layer for eddy fluxes of dry enthalpy
F_m	0.30	–	Moisture loading factor

Table 4.1: List of all constant parameters used in the simple model described in section 4.2.

Schneider (2008a) for the total kinetic energy. A nonmonotonic behavior was observed as well for eddy momentum fluxes in the deep tropics (Levine and Schneider, 2011).

4.3.3 Other constant parameters

The SLM depends on many geometrical and thermal parameters that are considered invariant to climate changes. Some of these parameters may be very precisely estimated, while others were tuned to provide an Earth-like reference climate when forced by Earth-like thermal and eddy parameters. These parameters and their values are listed in Table 4.1. In addition, the latitudinal profile for the gross moist stability (GMS) is prescribed to that diagnosed in the reference GCM simulations; this profile for the GMS vanishes at the equa-

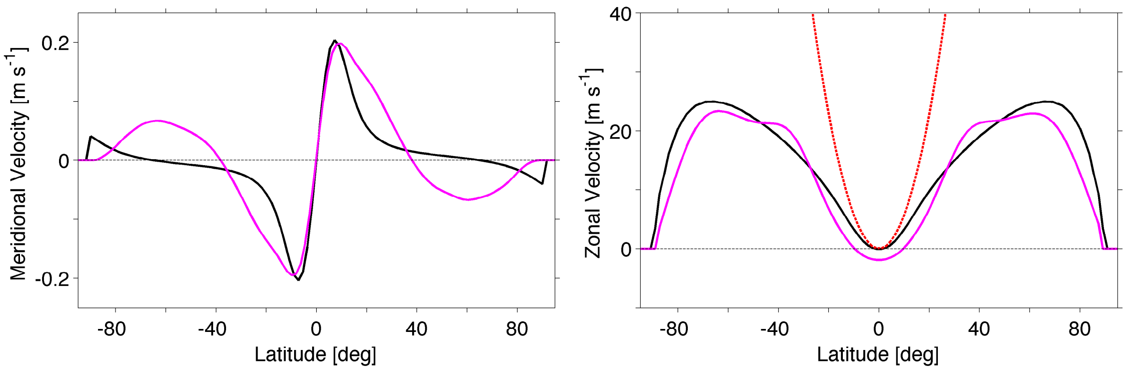

Figure 4.4: Meridional wind profile (left panel) and zonal wind profile (right panel) for the Earth-like reference simulation obtained in the GCM and SLM, as a function of latitude. SLM variables are indicated by a solid black line, and GCM variables by a solid magenta line. A dashed red line shows the zonal wind profile in the angular-momentum conserving regime.

tor, consistent with quasi-equilibrium prevailing locally, and increases near quadratically with latitude.

4.4 Results

4.4.1 Reference climate

Figure 4.4 shows the zonal wind and meridional mass flux profiles predicted by the SLM in the reference simulation, and compares them to their corresponding profiles in the (eddy-resolving) GCM simulations. Comparing GCM and SLM outputs is not straightforward, due to the highly truncated nature of the SLM: here, SLM outputs are compared to their respective mean fields in the GCM averaged from the $750\,\mathrm{hPa}$ pressure level to the top of the atmosphere. The $750\,\mathrm{hPa}$ pressure level corresponds to a region where the mean meridional wind nearly vanishes, and thus separates the strong equatorward mean mass flux in the boundary layer from the poleward mean mass flux in the upper layer.

On the left panel, the upper-layer mass flux obtained in the SLM is compared to the mean meridional mass flux in the GCM. The location and magnitude of the maximum strength are remarkably similar between both models. On the other hand, the latitude where mass flux reverses sign is significantly poleward in the SLM simulation compared to that in the corresponding GCM simulation. The meridional wind is found to be quite weak over a large region in the midlatitudes, its magnitude appears to be sensitive to poorly constrained processes implemented for numerical stability, such as Rayleigh damping for the zonal wind or eddy diffusivity for the meridional wind. These processes becomes rapidly negligible as the meridional wind strengthens. Hence, a more robust definition for the terminus of the Hadley circulation is to consider the latitude where the meridional wind is 10% of its maximum value, poleward of the location where this maximum is attained. This definition defines the terminus in a region where the large scale dynamics, either in the form of nonlinear advective fluxes or eddy fluxes, controls the meridional wind and its change with global climate changes. Using this definition, we find that the terminus is located at 21° latitude, which is much nearer to its location in the corresponding GCM simulation.

On the right panel, the upper-layer zonal wind in the SLM is compared to the mean zonal wind in the GCM. As for the meridional flow, the zonal wind profile shows strong similarities and some discrepancies. The magnitude of the maximum zonal wind is found to be comparable; however, the subtropical jet in the SLM is displaced significantly poleward of its location in the GCM, consistent with the zero crossing of the meridional wind being also shifted poleward. We also find an offset in the zonal wind profile: while the zonal wind

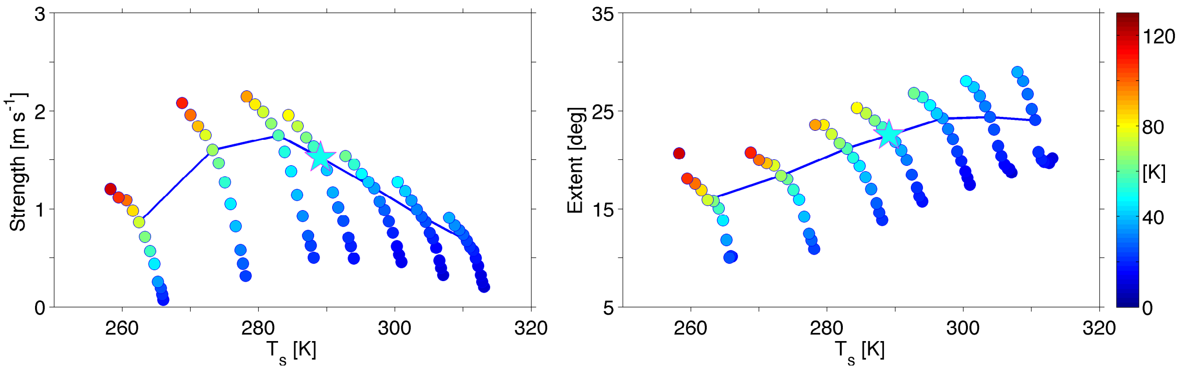

Figure 4.5: Strength (left panel) and extent of the Hadley circulation (right panel) in the moist GCM simulations (described in section 4.7.2), with respect to changes in the global-mean surface temperature and pole-to-equator temperature contrast. Changes in the strength and extent of the Hadley circulation shown by the blue line is extensively described in Levine and Schneider (2011), in particular the non-monotonicity of the strength and the steady widening of the cells with global warming. Plotting conventions are identical to those described in Fig. 4.3.

is exactly 0 in the SLM simulation at the equator, an easterly zonal wind develops in the GCM simulations, which is consistent with a local divergence of momentum by eddy fluxes there; in the SLM, on the other hand, eddy momentum flux divergence locally vanishes at the equator, consistent with zonal wind being null there.

The SLM captures the main dynamical features, when forced by adequate values for the thermal parameters (Fig. 4.2) and the eddy velocity (Fig. 4.3). In particular, the SLM captures the large departure of the zonal wind from either a radiative-convective equilibrium regime (no large-scale dynamics) or an angular-momentum conserving regime (no eddy fluxes).

4.4.2 Climate change experiments

Perhaps it is not surprising to find similarities in the reference simulation between the GCM and SLM since geometrical and thermal parameters (section 4.3.1) were tuned to provide a relatively good fit with the GCM simulation in this climate. To validate the relevance of the SLM to climate changes, thermal and eddy parameters are varied as in Figs. 4.2 and 4.3 to simulate large changes in longwave optical opacity and insolation contrast; corresponding simulations are obtained using the (eddy-resolving) GCM described in appendix 4.7.2.

Changes in the strength and extent of the Hadley circulation simulated by the GCM, when forced by a wide range of insolation contrasts and longwave optical opacities, are shown in Fig. 4.5. There, we observe that the Hadley circulation strengthens and widens as the insolation contrast increases. When increasing longwave optical opacity, its strength has a nonmonotonic behavior, peaking in magnitude near the reference simulation. The Hadley circulation also widens, consistent with the findings of Levine and Schneider (2011). Figure 4.6 shows that the SLM can reproduce nearly all the significant variations in the strength and extent of the Hadley circulation that are observed in the corresponding GCM simulations, apart from some quantitative deviations in the warmest climates. This is quite significant considering the simplicity of the SLM, in particular its axisymmetric nature and the crude representation of eddy fluxes.

4.4.3 Climate sensitivity experiments

The relative simplicity of the SLM allows us to investigate the sensitivity of the Hadley circulation to independent parameters; in particular, it is possible to test, as an independent variable, the effect of extratropical eddy activity on the strength and extent of the Hadley circulation with global climate change. Here, a series of simulations is performed in which every climate forcing parameter described in section 4.3 is varied independently.

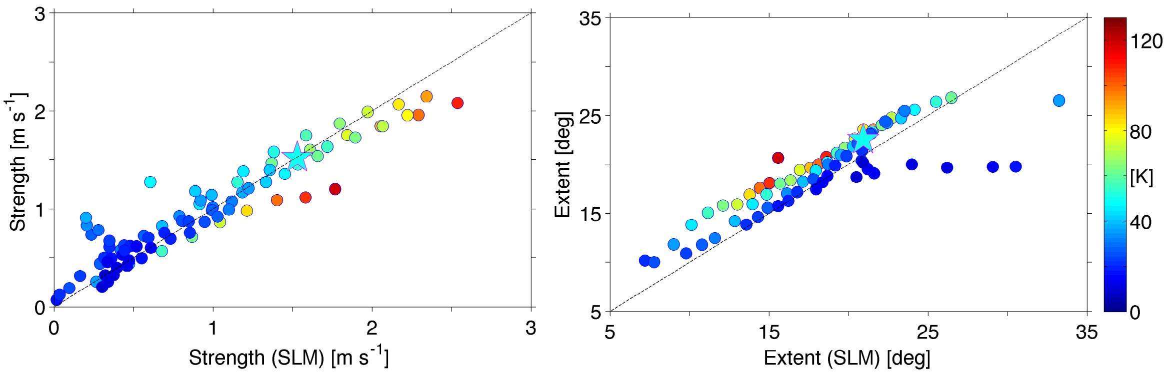

Figure 4.6: Strength (left panel) and extent of the Hadley circulation (right panel) in the moist GCM simulations shown on Fig. 4.5, and in a corresponding set of simulations obtained using the simple model described in section 4.2 (SLM). Climate is varied in the SLM by changing a set of thermal parameters, whose sensitivities to climate change are captured from a simple radiative-convective calculation depending only on longwave optical opacity and insolation, and by changing an eddy velocity, whose variations correspond to changes in the eddy activity and may be estimated from a GCM simulation (see section 4.3.2). Plotting conventions are identical to those described in Fig. 4.3. This figure shows that the SLM captures changes in the strength and extent of the Hadley circulation for a wide range of climate changes, varying both the insolation contrast and longwave optical opacity.

The contributions of changes in the tropopause height (Z_T), moisture factor (γ_r), and the eddy velocity (v_e) to changes in the strength and extent of the Hadley circulation may be decomposed as follows:

$$\begin{cases} \log \frac{\psi}{\psi^R} = \chi_1 \log \frac{Z_T}{Z_T^R} + \chi_2 \log \frac{\gamma_r}{\gamma_r^R} + \chi_3 \log \frac{\Delta T_{RC}}{\Delta T_{RC}^R} + \chi_4 \log \frac{v_e}{v_e^R}, \\ \\ \log \frac{\varphi}{\varphi^R} = \mu_1 \log \frac{Z_T}{Z_T^R} + \mu_2 \log \frac{\gamma_r}{\gamma_r^R} + \mu_3 \log \frac{\Delta T_{RC}}{\Delta T_{RC}^R} + \mu_4 \log \frac{v_e}{v_e^R}, \end{cases} \tag{4.56}$$

where

$$\chi_1 = \frac{\partial \log \psi}{\partial \log Z_T} \Big|^R_{\{\gamma_r;\Delta T_{RC};v_e\}} \quad \text{and} \quad \mu_1 = \frac{\partial \log \varphi}{\partial \log Z_T} \Big|^R_{\{\gamma_r;\Delta T_{RC};v_e\}}, \tag{4.57}$$

and

$$\chi_2 = \frac{\partial \log \psi}{\partial \log \gamma_r} |^R_{\{Z_T; \Delta T_{RC}; v_e\}} \quad \text{and} \quad \mu_2 = \frac{\partial \log \varphi}{\partial \log \gamma_r} |^R_{\{Z_T; \Delta T_{RC}; v_e\}}, \tag{4.58}$$

and

$$\chi_3 = \frac{\partial \log \psi}{\partial \log \Delta T_{RC}} |^R_{\{Z_T; \gamma_R; v_e\}} \quad \text{and} \quad \mu_3 = \frac{\partial \log \varphi}{\partial \log \Delta T_{RC}} |^R_{\{Z_T; \gamma_R; v_e\}}, \tag{4.59}$$

and

$$\chi_4 = \frac{\partial \log \psi}{\partial \log v_e} |^R_{\{Z_T; \gamma_R; \Delta T_{RC}\}} \quad \text{and} \quad \mu_4 = \frac{\partial \log \varphi}{\partial \log v_e} |^R_{\{Z_T; \gamma_R; \Delta T_{RC}\}} \tag{4.60}$$

are the exponents in a power law relating the strength and extent of the Hadley circulation to changes in tropopause height, moisture sensitivity to temperature, and radiative-convective temperature contrast, and eddy velocity respectively. Here, $(.)^R$ defines the Earth-like reference simulation. The decomposition shown in Eqn. 4.56, which applies strictly to relatively small changes in the strength and extent around the reference climate, can be summarized as follows:

$$\begin{cases} \psi \sim Z_T^{\chi_1} \, \gamma_r^{\chi_2} \, \Delta T_{RC}^{\chi_3} \, v_e^{\chi_4}, \\ \\ \varphi \sim Z_T^{\mu_1} \, \gamma_r^{\mu_2} \, \Delta T_{RC}^{\mu_3} \, v_e^{\mu_4}. \end{cases} \tag{4.61}$$

Estimates for these coefficients are shown in Table 4.2.

Strength	(Exponent)	Extent	(Exponent)	Definition
χ_1	0.6	μ_1	0.3	Sensitivity to tropopause height changes (Z_T)
χ_2	-0.4	μ_2	0	Sensitivity to moisture content changes (γ_r)
χ_3	1.0	μ_3	0.2	Sensitivity to thermal contrast changes (ΔT_{RC})
χ_4	-0.1	μ_4	0	Sensitivity to eddy activity changes (v_e)

Table 4.2: Sensitivity coefficients, computed from the SLM, for the strength and extent of the Hadley circulation to changes in external forcing parameters, for perturbations around the reference simulation shown in Fig. 4.4. These coefficients are defined in Eqn. 4.56.

Perhaps the most striking feature shown on Table 4.2 is the relative invariance of the strength and extent to changes in the eddy activity, despite the latter changing by relatively large amounts as climate changes (as shown on Fig. 4.3). On the other hand, changes in thermal forcing parameters appear to be paramount for driving changes experienced by the strength and terminus with global climate changes. An increase in either the tropopause height or the pole-to-equator thermal contrast leads to a widening and strengthening of the cell, while an increase in the moisture sensitivity factor weakens the Hadley circulation. The nonmonotonic behavior of the strength with global warming observed in Levine and Schneider (2011) is ascribed to a lifting of the tropical tropopause, which strengthens the Hadley circulation in cold climates; in warm climates, this is offset by a rapid increase in the lower-tropospheric moisture content as climate warms, which acts to weaken the Hadley circulation. The steady widening of the circulation with global warming, on the other hand, can be attributed to a steady lifting of the tropopause, as shown on Fig. 4.2.

4.5 Discussion

Section 4.4 contains intriguing results, which may potentially conflict with existing theories. The sensitivity analysis shown in Table 4.2 suggests that the lifting of the tropopause height leads to a widening of the circulation[1]. This behavior is consistent with previous studies, linking global warming and a lifting of the tropopause (e.g., Santer et al., 2003). The value of the exponent for the sensitivity of the extent to changes in tropopause height (0.3) is significantly lower than its value (0.5) predicted in the angular momentum-conserving scenarios (cf. Held and Hou, 1980), confirming that eddy fluxes are significant in setting the extent of the Hadley circulation and its sensitivity to global climate changes. This exponent for the tropopause height is comparable to that predicted by an angular momentum-conserving circulation terminated by baroclinic instability (Held, 2000), for which an exponent equal to 0.25 was found. This relative agreement could explain, in particular, the relative success of this scaling when applied to climate changes of modest amplitudes (Lu et al., 2007; Frierson et al., 2007; Korty and Schneider, 2008; Kang and Lu, 2012). However, the widening of the Hadley circulation does not explicitly depend on the local static stability at the terminus of the Hadley circulation. Although not being inconsistent with a potential increase in the subtropical and extratropical static stability, our finding seems to contradict the hypothesis that the widening of the cells in global warming scenarios, around the reference climate, is caused by a local increase in the static stability at the

---

[1] It is important to note, however, that a steady widening of the Hadley circulation is not always accompanied by a lifting of the tropopause, unlike what the SLM suggests: a potent counterexample is an ENSO-type climate change. During an El-Niño (La Niña) event, the terminus of the cells shifts equatorward (poleward) despite the tropical tropopause shifting upward (downward) and the pole-to-equator temperature contrast increasing (decreasing). This response is not captured by the SLM, which suggests that one of the assumption of the SLM may not hold for all kinds of climate changes, despite it providing decent results when simulating the dynamical response of the circulation to changes in longwave optical opacity and insolation contrast.

terminus (Walker and Schneider, 2006; Frierson et al., 2007). Rather, our results suggest that, for climate changes around the reference simulation, the static stability at the terminus will adjust to changes in its location and low-level shear, whose changes appear to be set primarily by the direct response of the Hadley circulation to a lifting of the tropopause. In other words, our findings suggest that the subtropical static stability responds to a widening induced by changes in thermal forcings, and not vice versa.

Table 4.2 implies that the strength of the Hadley circulation responds primarily to changes in the tropopause height and in the moisture content, at least near the reference climate. The weakening of the Hadley circulation with global warming in the SLM differs from the theory proposed by Held and Soden (2006) for the weakening in the Walker circulation with global warming; there, it was found that slower changes in precipitation compared to the static stability would lead to a weakening of the Walker cell. This argument, which was found to be a poor predictor for changes in the strength of the Hadley circulation (Schneider et al., 2010), is not consistent with the thermodynamic budget of the SLM (Eqn. 4.23): there, convective precipitation in the deep tropics has no direct effect on the strength of the circulation, insofar as the gross moist static stability remains invariant. Instead, we find that the increase in moisture transport by eddies weakens the Hadley circulation as climate warms. This increase in eddy moisture flux with global warming is due to a steep increase in the low-tropospheric moisture content offsetting a concomitant reduction in eddy activity. This weakening tendency by an increased water vapor content is opposed by a strengthening of the circulation by a lifting of the tropopause height; this opposed tendencies lead to a nonmonotonicity with global warming, as shown on Fig 4.5, regardless of the concomitant nonmonotonicity in the eddy velocities.

4.6 Conclusions

We have devised a reduced dynamical model of the troposphere, which accounts separately for the direct thermal forcings and indirect eddy forcings on the mean meridional circulation, to investigate changes in the Hadley circulation with global climate changes and compare those to existing theories. We found that this model captures relatively well changes in the strength and extent of the Hadley circulation over a wide range of climate changes. We then performed a sensitivity study, changing every external parameter one at a time, and find that changes in the strength and extent are remarkably insensitive to changes in eddy activity for small climate changes around the reference climate. While the strength is sensitive mostly to a lifting of the tropopause height (strengthening), and an increase in the tropospheric moisture content (weakening), the extent has a strong dependence on the tropopause height (widening), as global climate warms. Both the strength and the extent are sensitive to changes in insolation contrasts, leading to a strengthening and widening of the cells with a steepening of the insolation profile.

4.7 Appendix

4.7.1 Numerics

To ensure numerical stability, the three prognostic variables of the model ($u_t; v_t; \langle T \rangle$) are solved on a staggered grid, with u_t and $\langle T \rangle$ being solved at locations nested in between those of v_t, following the code developed by Sobel and Schneider (2009). Meridional advection terms are computed using an upwind scheme. The domain has a width of 4 planetary radii in each hemisphere, although the insolation forcing is applied only on the centermost 1-radii section of the domain. At the boundaries of the domain, meridional and zonal winds are set to 0. The model is integrated for a total of 75 days for each simulation; a steady state is generally achieved at 60 days and beyond, and no time averages are performed on the outputs.

4.7.2 General circulation model (GCM)

The idealized GCM is extensively described in O'Gorman and Schneider (2008b), and only a brief overview is provided here. The GCM solves for the primitive equations on a sphere; the atmosphere is assumed to be in hydrostatic balance; Water vapor is advected by the flow, and may condense when its local concentration exceeds saturation. A simple quasi-equilibrium convection scheme represents the effect of deep and shallow convection on the thermodynamic and water budgets of the atmosphere. In the boundary layer, a Monin-Obhukov diffusive scheme enhance the mixing as a result of greater mechanical and thermal forcing there.

A quadratic insolation profile is prescribed at the top of the atmosphere. Both shortwave and longwave radiation are absorbed by the atmosphere and at the surface; while absorption depends only on the prescribed atmospheric optical opacity and surface albedo for shortwave radiation, absorption of longwave radiation is a function of both temperature and longwave optical opacity.

To ease comparison between our radiative-convective equilibrium and full dynamical simulations, we construct a radiative-convective model of the atmosphere from the same idealized moist GCM used for the climate change experiment described above. A radiative-convective equilibrium is obtained by turning off all meridional fluxes in the GCM. A constant value for the zonal wind velocity ($\overline{u} = 2\,\mathrm{m\,s^{-1}}$) is prescribed everywhere to allow for surface fluxes.

Chapter 5

Conclusions

This thesis provides a comprehensive description of the Hadley circulation and how it responds to climate changes. It discusses how the Hadley circulation strength and extent can change.

In the first chapter, we describe the Hadley circulation in a global warming experiment centered around an Earth-like reference simulation, which encompasses both extremely cold and warm climates: while the Hadley circulation terminus shifts poleward as climate warms, its strength is found to vary nonmonotonically, peaking in a climate close to the reference simulation (see also O'Gorman and Schneider, 2008b). The widening rate of the Hadley circulation, however, is found to depend sensitively on the actual definition of the terminus. Adding a simple representation of a wind-driven ocean overturning circulation to the moist idealized GCM, we find significant differences in the response of the Hadley circulation: Ocean heat transport substantially weakens the strength of the Hadley circulation (by up to 50%), and marginally widens the cells. These effects are largest in cold climates and decrease as the climate warms, consistent with a steady decrease in the meridional temperature gradient at the surface. We find that eddy stress on the mean zonal flow varies greatly over this range of climate in the deep tropics, showing a nonmonotonic behavior similar to that of the strength of the Hadley circulation. This is consistent with a nonmonotonicity in the midlatitude mean available potential energy (O'Gorman and Schneider, 2008a). The influence of this eddy stress on the dynamics, however, decreases steadily with global warming, implying the circulation becomes progressively thermally driven as climate warms.

In the second chapter, we modify an existing criterion, supercriticality, which compares the depth of baroclinic waves to that of the troposphere (Schneider and Walker, 2006), to account for convective adjustments in synoptic updrafts. We apply this criterion to a large set of idealized GCM simulations to characterize the degree of control exerted by baroclinic waves in the storm track regions as well as at the terminus of the Hadley circulation. This set of GCM simulations encompasses both dry and moist atmospheres, spanning a wide range of global-mean temperatures and pole-to-equator thermal contrasts. We confirm that the terminus of the Hadley circulation defines the equatorward edge of a region of deep baroclinic waves. The location of the terminus is always below 35° latitude, regardless of the thermal forcing, which suggests a maximum bound for the extent of the Hadley circulation on a planet with Earth-like orbital and thermal parameters. Although baroclinic waves appear to always control the tropospheric static stability at the terminus of the Hadley circulation in dry atmospheres, this does not always hold in moist atmospheres: there, scenarios of very warm and weakly differentially heated climates are not characterized by this property.

In the third chapter, we devise a single-layer axisymmetric model (SLM). In this model, the effects of moisture and eddies on the thermodynamic and momentum budgets of the atmosphere are parameterized with closures. We vary independently a set of thermal parameters and an eddy activity factor to change climates. We find that this model captures variations in the strength and extent of the Hadley circulation over a wide range of climates. Preliminary results suggests that these changes may be attributed primarily to its response to changes in the direct thermal forcing parameters: the lifting of the tropical tropopause and increase in the moisture content driven by global warming.

Bibliography

Arakawa, A. and W. H. Schubert, 1974: Interaction of a cumulus cloud ensemble with the large-scale environment, Part I. *J. Atmos. Sci.*, **31**, 674–701.

Archer, C. L. and K. Caldeira, 2008: Historical trends in the jet streams. *Geophys. Res. Lett.*, **35**, L08 803.

Becker, E. and G. Schmitz, 2001: Interaction between extratropical stationary waves and the zonal mean circulation. *J. Atmos. Sci.*, **58 (5)**, 462–480.

Bordoni, S. and T. Schneider, 2008: Monsoons as eddy-mediated regime transitions of the tropical overturning circulation. *Nature Geos.*, **1**, 515–519.

Bourke, W., 1974: A multi-level spectral model. I. Formulation and hemispheric integrations. *Mon. Wea. Rev.*, **102**, 687–701.

Caballero, R., 2007: Role of eddies in the interannual variability of Hadley cell strength. *Geophys. Res. Lett.*, **34**, L22 705.

Caballero, R., 2008: Hadley cell bias in climate models linked to extratropical eddy stress. *Geophys. Res. Lett.*, **35**, L18 709.

Caballero, R. and M. Huber, 2010: Spontaneous transition to superrotation in warm climates simulated by CAM3. *Geophys. Res. Lett.*, **37 (11)**, L11 701.

Chen, J., B. E. Carlson, and A. D. Del Genio, 2002: Evidence for strengthening of the tropical general circulation in the 1990s. *Science*, **295**, 838–841.

Dickinson, R. E., 1971: Analytic model for zonal winds in the tropics. *Mon. Wea. Rev.*, **99**, 511–523.

Dima, I. M. and J. M. Wallace, 2003: On the seasonality of the Hadley cell. *J. Atmos. Sci.*, **60**, 1522–1527.

Emanuel, K. A., 1985: Frontal circulations in the presence of small moist symmetric stability. *J. Atmos. Sci.*, **42**, 1062–1071.

Frierson, D. M. W., 2007: The dynamics of idealized convection schemes and their effect on the zonally averaged tropical circulation. *J. Atmos. Sci.*, **64**, 1959–1976.

Frierson, D. M. W., I. M. Held, and P. Zurita-Gotor, 2006: A gray-radiation aquaplanet moist GCM. Part I: Static stability and eddy scale. *J. Atmos. Sci.*, **63**, 2548–2566.

Frierson, D. M. W., J. Lu, and G. Chen, 2007: The width of the Hadley cell in simple and comprehensive general circulation models. *Geophys. Res. Lett.*, **34**, L18 804.

Gasse, F. and C. N. Roberts, 2004: *The Hadley Circulation: Past, Present, and Future*, chap. 11. Late Quaternary hydrologic changes in the arid and semiarid belt of northern Africa: Implications for past atmospheric circulation, 313–345. Springer.

Haynes, P. H., M. E. McIntyre, T. G. Shepherd, C. J. Marks, and K. P. Shine, 1991: On the downward control of extratropical diabatic circulations by eddy-induced mean zonal forces. *J. Atmos. Sci.*, **48**, 651–678.

Held, I. M., 1978: The vertical scale of an unstable baroclinic wave and its importance for eddy heat flux parameterizations. *J. Atmos. Sci.*, **35**, 572–576.

Held, I. M., 1982: On the height of the tropopause and the static stability of the troposphere. *J. Atmos. Sci.*, **39**, 412–417.

Held, I. M., 2000: The general circulation of the atmosphere. *Proc. Prog. Geophys. Fluid Dyn.*, Woods Hole Oceanogr. Inst, Wodds Hole, MA, 70, http://gfd.whoi.edu/proceedings/2000/PDFvol2000.html.

Held, I. M., 2001: The partitioning of the poleward energy transport between the tropical ocean and atmosphere. *J. Atmos. Sci.*, **58**, 943–948.

Held, I. M. and A. Y. Hou, 1980: Nonlinear axially symmetric circulations in a nearly inviscid atmosphere. *J. Atmos. Sci.*, **37**, 515–533.

Held, I. M. and B. J. Soden, 2006: Robust responses of the hydrological cycle to global warming. *J. Climate*, **19**, 5686–5699.

Herweijer, C., R. Seager, M. Winton, and A. Clement, 2005: Why ocean heat transport warms the global mean climate. *Tellus A*, **57**, 662–675.

Hu, Y. and Q. Fu, 2007: Observed poleward expansion of the Hadley circulation since 1979. *Atmos. Chem. Phys.*, **7**, 5229–5236.

Hudson, R. D., M. F. Andrade, M. B. Follette, and A. D. Frolov, 2006: The total ozone field separated into meteorological regimes–Part II: Northern Hemisphere mid-latitude total ozone trends. *Atmos. Chem. Phys*, **6**, 5183–5191.

Johanson, C. and Q. Fu, 2009: Hadley cell widening: Model simulations versus observations. *J. Climate*, **22**, 2713–2725.

Kallberg, P., A. Simmons, S. Uppala, and M. Fuentes, 2004: The ERA-40 archive. *ERA-40 Project Report Series*, Reading, UK, ECMWF, 31, 17.

Kang, S. M. and J. Lu, 2012: Expansion of the Hadley cell under global warming: winter versus summer. *J. Climate*.

Kim, H. and S. Lee, 2001: Hadley cell dynamics in a primitive equation model. Part II: Nonaxisymmetric flow. *J. Atmos. Sci.*, **58**, 2859–2871.

Klinger, B. A. and J. Marotzke, 2000: Meridional heat transport by the subtropical cell. *J. Phys. Oceanogr.*, **30**, 696–705.

Korty, R. L. and T. Schneider, 2008: Extent of Hadley circulations in dry atmospheres. *Geophys. Res. Lett.*, **35**, L23 803.

Lapeyre, G. and I. M. Held, 2004: The role of moisture in the dynamics and energetics of turbulent baroclinic eddies. *J. Atmos. Sci*, **61**, 1693–1710.

Lee, M. I., M. J. Suarez, I. S. Kang, I. M. Held, and D. Kim, 2008: A moist benchmark calculation for atmospheric general circulation models. *J. Climate*, **21**, 4934–4954.

Levine, X. J. and T. Schneider, 2011: Response of the Hadley circulation to climate change in an aquaplanet GCM coupled to a simple representation of ocean heat transport. *J. Atmos. Sci.*, **68**, 769–782.

Lindzen, R. S. and A. V. Hou, 1988: Hadley circulations for zonally averaged heating centered off the equator. *J. Atmos. Sci.*, **45**, 2416–2427.

Lu, J., G. A. Vecchi, and T. Reichler, 2007: Expansion of the Hadley cell under global warming. *Geophys. Res. Lett.*, **34**, L06 805.

Lu, P., J. P. McCreary Jr., and B. A. Klinger, 1998: Meridional circulation cells and the source waters of the Pacific equatorial undercurrent. *J. Phys. Oceanogr.*, **28**, 62–84.

McCreary Jr., J. P. and P. Lu, 1994: Interaction between the subtropical and equatorial ocean circulations: the subtropical cell. *J. Phys. Oceanogr.*, **24**, 466–497.

Mitas, C. M. and A. Clement, 2005: Has the Hadley cell been strengthening in recent decades? *Geophys. Res. Lett.*, **32**, L03 809.

Mitchell, J. L., R. T. Pierrehumbert, D. M. W. Frierson, and R. Caballero, 2006: The dynamics behind titan's methane clouds. *Proc. Natl. Acad. Sci. USA*, **103**, 18 421–18 426.

O'Gorman, P. A., 2010: The effective static stability experienced by eddies in a moist atmosphere. *J. Atmos. Sci.*, 1–15.

O'Gorman, P. A. and T. Schneider, 2008a: Energy of midlatitude transient eddies in idealized simulations of changed climates. *J. Climate*, **21**, 5797–5806.

O'Gorman, P. A. and T. Schneider, 2008b: The hydrological cycle over a wide range of climates simulated with an idealized GCM. *J. Climate*, **21**, 3815–3832.

O'Gorman, P. A. and T. Schneider, 2008c: Weather-layer dynamics of baroclinic eddies and multiple jets in an idealized general circulation model. *J. Atmos. Sci.*, **65**, 524–535.

Peixoto, J. P. and A. H. Oort, 1992: *Physics of Climate*. American Institute of Physics, New York, 520 pp.

Phillips, N. A., 1954: Energy transformations and meridional circulations associated with simple baroclinic waves in a two-level, quasi-geostrophic model. *Tellus*, **6**, 273–286.

Quan, X. W., H. F. Diaz, and M. P. Hoerling, 2004: *The Hadley circulation: Past, present, and future*, chap. 3. Change in the tropical Hadley cell since 1950, 85–120. Springer.

Ralph, F. M., P. J. Neiman, and G. A. Wick, 2004: Satellite and caljet aircraft observations of atmospheric rivers over the eastern north pacific ocean during the winter of 1997/98. *Mon. Wea. Rev.*, **132**, 1721–1745.

Reichler, T., 2009: *Climate Change: Observed Impacts on Planet Earth*, chap. 7. Changes in the atmospheric circulation as indicator of climate change, 145–164. Elsevier Science.

Rosenlof, K. H., 2002: Transport changes inferred from HALOE water and methane measurements. *J. Meteor. Soc. Japan*, **80**, 831–848.

Santer, B. D., et al., 2003: Contributions of anthropogenic and natural forcing to recent tropopause height changes. *Science*, **301**, 479–483.

Santer, B. D., et al., 2005: Amplification of surface temperature trends and variability in the tropical atmosphere. *Science*, **309**, 1551–1556.

Schneider, E. K., 1977: Axially symmetric steady-state models of the basic state for instability and climate studies. Part II. Nonlinear calculations. *J. Atmos. Sci.*, **34**, 280–296.

Schneider, T., 2004: The tropopause and the thermal stratification in the extratropics of a dry atmosphere. *J. Atmos. Sci.*, **61**, 1317–1340.

Schneider, T., 2006: The general circulation of the atmosphere. *Annu. Rev. Earth Planet. Sci.*, **34**, 655–688.

Schneider, T. and S. Bordoni, 2008: Eddy-mediated regime transitions in the seasonal cycle of a Hadley circulation and implications for monsoon dynamics. *J. Atmos. Sci.*, **65**, 915–934.

Schneider, T., S. D. B. Graves, E. L. Schaller, and M. E. Brown, 2012: Polar methane accumulation and rainstorms on titan from simulations of the methane cycle. *Nature*, **481**, 58–61.

Schneider, T. and J. Liu, 2009: Formation of jets and equatorial superrotation on Jupiter. *J. Atmos. Sci.*, **66**, 579–601.

Schneider, T. and P. A. O'Gorman, 2008: Moist convection and the thermal stratification of the extratropical troposphere. *J. Atmos. Sci.*, **65**, 3571–3583.

Schneider, T., P. A. O'Gorman, and X. J. Levine, 2010: Water vapor and the dynamics of climate changes. *Rev. Geophys.*, **48**, 1–22.

Schneider, T. and C. C. Walker, 2006: Self-organization of atmospheric macroturbulence into critical states of weak nonlinear eddy–eddy interactions. *J. Atmos. Sci.*, **63**, 1569–1586.

Schneider, T. and C. C. Walker, 2008: Scaling laws and regime transitions of macroturbulence in dry atmospheres. *J. Atmos. Sci.*, **65**, 2153–2173.

Seager, R., et al., 2007: Model projections of an imminent transition to a more arid climate in southwestern North America. *Science*, **316**, 1181–1184.

Seidel, D. J., Q. Fu, W. J. Randel, and T. J. Reichler, 2008: Widening of the tropical belt in a changing climate. *Nature Geosci.*, **1**, 21–24.

Seidel, D. J. and R. J. Randel, 2007: Recent widening of the tropical belt: Evidence from tropopause observations. *J. Geophys. Res.*, **112**, D20 113.

Sherwood, S. C., 2007: Simultaneous detection of climate change and observing biases in a network with incomplete sampling. *J. Climate*, **20**, 4047–4062.

Simmons, A. J. and D. M. Burridge, 1981: An energy and angular-momentum conserving vertical finite-difference scheme and hybrid vertical coordinates. *Mon. Wea. Rev.*, **109**, 758–766.

Sobel, A. H., J. Nilsson, and L. M. Polvani, 2001: The weak temperature gradient approximation and balanced tropical moisture waves. *J. Atmos. Sci.*, **58**, 3650–3665.

Sobel, A. H. and T. Schneider, 2009: Single-layer axisymmetric model for a Hadley circulation with parameterized eddy momentum forcing. *JAMES*, **1**, 11 pp.

Stofan, E. R., et al., 2007: The lakes of titan. *Nature*, **445**, 61–64.

Stone, P. H., 1978: Baroclinic adjustment. *J. Atmos. Sci*, **35**, 561–571.

Tanaka, H. L., N. Ishizaki, and D. Nohara, 2005: Intercomparison of the intensities and trends of Hadley, Walker and monsoon circulations in the global warming projections. *SOLA*, **1**, 77–80.

Trenberth, K. E. and J. M. Caron, 2001: Estimates of meridional atmosphere and ocean heat transports. *J. Climate*, **14**, 3433–3443.

Trenberth, K. E. and A. Solomon, 1994: The global heat balance: Heat transports in the atmosphere and ocean. *Clim. Dyn.*, **10**, 107–134.

Trenberth, K. E. and D. P. Stepaniak, 2003: Seamless poleward atmospheric energy transports and implications for the Hadley circulation. *J. Climate*, **16**, 22.

Uppala, S. M., et al., 2005: The ERA-40 re-analysis. *Quart. J. Roy. Meteor. Soc*, **131**, 2961–3012.

Walker, C. C. and T. Schneider, 2005: Response of idealized Hadley circulations to seasonally varying heating. *Geophys. Res. Lett.*, **32**, L06 813.

Walker, C. C. and T. Schneider, 2006: Eddy influences on Hadley circulations: Simulations with an idealized GCM. *J. Atmos. Sci.*, **63**, 3333–3350.

Xian, P. and R. L. Miller, 2008: Abrupt seasonal migration of the ITCZ into the Summer Hemisphere. *J. Atmos. Sci.*, **65**, 1878–1895.